TIROS III
RADIATION DATA USERS'
MANUAL SUPPLEMENT

NASA

GODDARD SPACE FLIGHT CENTER
GREENBELT, MARYLAND

TIROS III
RADIATION DATA USERS'
MANUAL SUPPLEMENT

Correction Models for Instrumental Response Degradation

W. R. Bandeen
R. E. Samuelson
I. Strange

Aeronomy and Meteorology Division
Goddard Space Flight Center
NATIONAL AERONAUTICS AND SPACE ADMINISTRATION
Greenbelt, Maryland

December 1, 1963

TABLE OF CONTENTS

LIST OF FIGURES

LIST OF TABLES

LIST OF SYMBOLS

Note: This list includes symbols which are used more than once in the text. Symbols which are used and defined at only one point in the text are not repeated below.

A^c Cumulative quasi-global albedo from measurements, including any effects of degradation

C Symmetrical degradation constant for both floor and wall sides of a radiometer channel

C^r Degradation constant for the floor side

C^w Degradation constant for the wall side

f Transmittance of lens-filter combination

Δf The flight measured space-viewed level minus the ground calibrated "space-viewed" level (c.p.s.)

F_{sc} Output frequency of a voltage controlled oscillator (c.p.s.)

i Orbit Number

I Absorbed insolation ($g\ cal\ cm^{-2}\ min^{-1}$)

j Arbitrary number of orbits from orbit i

k Constant of proportionality relating V_{RAD} and $\overline{W}'$

m Specific number of orbits containing data

n Specific number of orbits containing data; n is larger than m

NA_{test} Maximum value of the minimum sensor nadir angle occurring in a swath required for the data in the swath to be accepted for processing (degrees)

N Radiance (watts meter^{-2} steradian^{-1})

N_λ Spectral radiance (watts meter^{-2} steradian^{-1} micron^{-1})

$\overline{N}$ Effective radiance to which an undegraded sensor responds, viz.,

$$\overline{N} = \int_0^\infty N_\lambda\, \phi_\lambda{}^*\, d\lambda$$

p An individual measurement of either total outgoing long wave radiant emittance or reflectance of solar radiation assigned to an applicable compartment in the multivariate distribution matrix

P^c Cumulative quasi-global emitted radiant power (watts) from measurements, including any effects of degradation

P^i Quasi-global emitted radiant power at orbit i, averaged over $\sim$ 20 orbits containing data in a chronological sequence of $\sim$ 50 orbits and assumed to prevail at the midpoint between the first $(i - j)$ and the last $(i + j)$ orbit in the sequence, from measurements, including any effects of degradation

$\overline{P}^i$ Quasi-global effective emitted radiant power at orbit i from measurements, including any effects of degradation

q The number of individual measurements in a compartment of the multivariate distribution matrix

Q Zonal illuminated area cross-section (meter^2) (See Fig. 7)

r	Reflectance of solar radiation, viz., $\overline{W}/\overline{W}^* \cos\theta_\odot$
r'	Reflectance calculated from a measurement that may be degraded
R	Reflectivity
R_e	Radius of the earth (6.3712×10^6 meters)
S	Solar Constant (2.0 g cal cm^{-2} min^{-1} $= 1395$ watts meter^{-2})
t	Time
T_{BB}	Equivalent blackbody temperature ($^\circ K$)
T_{BB}'	Measured equivalent blackbody temperature by a radiometer channel whose response may be degraded
ΔT_{BB}	T_{BB} (computed theoretically) minus T_{BB}' (measured)
δT_{BB}	Degradation correction term to be added algebraically to T_{BB}'
T_c	Radiometer housing temperature
T_E	Satellite electronics temperature
V_{RAD}	Output voltage from the radiometer
W	Radiant emittance (watts meter^{-2})
W_λ	Spectral radiant emittance (watts meter^{-2} micron^{-1})
$\overline{W}$	Effective radiant emittance, assuming isotropic radiation, to which an undegraded sensor responds, viz., $\overline{W} = \int_0^\infty W_\lambda \, \phi_\lambda^* \, d\lambda$ (For isotropic radiation, as in the calibration of the radiometer, $\overline{W} = \pi \overline{N}$)
$\overline{W}'$	Measured effective radiant emitance by a sensor whose response may be degraded
$\overline{W}_{ave}{}^i$	Average quasi-global effective radiant emittance $= (1/4.1785 \times 10^{14}) \; \overline{P}^i$, from measurements, including any effects of degradation
$\overline{W}^*$	"Effective solar constant" (i.e., the value of $\overline{W}$ which would be measured by an undegraded reflected solar radiation channel if the spot viewed were a perfectly diffuse reflector, having unit reflectivity, and illuminated at normal incidence by the solar constant)
α	Absorptivity of the thermistor bolometer
ε	Emissivity
ζ	Earth latitude (degrees)
η	Radiometer sensor nadir angle (degrees)
θ	Zenith angle (degrees)
$\theta_\odot$	Solar zenith angle
κ	Degradation "normalizing factor" by which $\overline{W}'$ measured by a reflected solar radiation channel is to be multiplied to normalize the data to Reference 3 (London)
λ	Wavelength (microns)
ϕ_λ^*	Effective spectral response function of an undegraded radiometer channel at the time of its calibration

ϕ_λ Effective spectral response function of a radiometer channel after its calibration and, hence, when it is possibly degraded (Note: The symbol "ϕ_λ" as used in the TIROS III Radiation Data Users' Manual is equivalent to "$\phi_\lambda{}^*$" as used in this Supplement)

ψ Azimuthal angle (degrees)

( )   distinguishes a second subscript or superscript

Subscripts:

   ave   average

   max   maximum

   min   minimum

Superscripts:

   ′   indicates a measurement by a radiometer channel whose response may be degraded

   b   black half of radiometer chopper

   F   floor side

   i   orbit number

   m   mirrored half of radiometer chopper

   s   "satellite," referring to assumption that all radiometer components exist at a common satellite interior temperature

   W   wall side

ERRATUM IN THE
"TIROS III RADIATION DATA CATALOG"

The base grid point for the map on page 90 (N 45.0, E 85.0) is actually the *next-to-the-top* grid point instead of the top grid point which is erroneously designated. The corresponding grid point in the extreme left-hand column of the map on page 91 is, consequently, also in error and the "box" should be moved down one grid point.

FOREWORD

This Supplement pertains to information contained in the "TIROS III Radiation Data Users' Manual" and the "TIROS III Radiation Data Catalog" and is intended to be used in conjunction with the two parent documents.

Specifically this Supplement is designed to serve as an aid in the interpretation of medium resolution radiation data from the TIROS III Meteorological Satellite through the application of correction models for the degradation in response which apparently occurred in the five-channel radiometer. More generally, it is intended to serve as a foundation on which to base subsequent investigations of the degradation of TIROS-like radiometers.

Many members of the Aeronomy and Meteorology Division made contributions in the calculations of data used in this Supplement, and their efforts are hereby acknowledged.

ABSTRACT

After publication of the "TIROS III Radiation Data Users' Manual" and its companion volume the "TIROS III Radiation Data Catalog," additional evidence concerning the apparent degradation of the response of the five-channel, medium resolution radiometer was discovered. This Supplement to the "TIROS III Radiation Data Users' Manual" discusses the additional evidence arising from several different investigations utilizing the data and elaborates on the discussion of instrumental degradation in Section VI of the TIROS III Manual.

The degradation in the instrumental response may be classified broadly into two types, based on the method of detection. One type of degradation was evidenced by a shift in the space-viewed level which increased with time and was accompanied by the appearance of distinctive "negative-going pulses" in that part of the analog signal corresponding to a scan across the horizon. This type of degradation was definitely observed only in the infrared channels 1 and 4 and occurred at different times after launch for the two channels.

The second type of degradation became apparent shortly after launch for all channels (except, perhaps, for channel 1 where the rapid development of the first type of degradation masked any development of the second). This type of degradation was characterized by a decrease in the overall response of the channel with time, without any shift in the space-viewed level or accompanying negative-going pulses, and was especially noticeable in the short wave channels, 3 and 5. Its discovery resulted from an attempt to make a study of the heat balance of the Earth when it was noticed that both the outgoing long wave radiative flux and the albedo over the quasi-globe (the broad zonal region between latitudes N55°-S55°) steadily decreased with time. (TIROS II and TIROS IV data also show the same characteristics.)

In this Supplement suggested correction nomograms are given for all channels, followed by a rather complete development of the degradation models which were used in their construction. The types, magnitudes, and possible causes of degradation are discussed in some detail. The models considered are of necessity somewhat idealized and, therefore, approximate. The resulting correction nomograms, pending further investigation, represent the best estimates of the authors for degradation corrections as of this writing but should by no means be considered as final.

xi

I. INTRODUCTION

In the "TIROS III Radiation Data Users' Manual"[1] (hereinafter called the "Manual") the statement is made that the infrared data are valid to orbits 118, 875, and 130 for channels 1, 2, and 4 respectively, after which degradation becomes appreciable.

For channels 1 (6.0-6.5μ) and 4 (8.0-30.0μ) the onset of appreciable degradation was indicated by a shift in the analog signal level occurring when outer space was viewed simultaneously by both directions of the radiometer (the "space-viewed level"), accompanied by characteristic "negative-going pulses" as the radiometer field of view scanned on and off the earth. This type of degradation may be termed "asymmetrical optical degradation".

For channel 2 (8.0-12.0μ) the onset of appreciable degradation was indicated by an increasing and excessive amount of system noise superimposed upon the analog signal, and only at a very late date (after orbit 875) did the asymmetrical characteristics associated with the other two infrared channels become barely detectable.

In the Manual the statement was made regarding channel 5 (0.55-0.75μ) that *"immediately after launch it is estimated that the absolute accuracy was ± 10 w/m²"*. Because of an observed pre-launch decrease in sensitivity of channel 3 (0.2-6.0μ), no estimates of absolute accuracy for channel 3 were given.

Subsequent analyses of the data from the TIROS III radiometer, as well as from TIROS II and IV, have given a greater insight into the behavior of the sensors while in orbit, giving strong evidence that the response characteristics of *all channels* degrade rapidly, beginning around the time of launch or shortly thereafter. This initial degradation is not accompanied by a shift in the space-viewed level or by negative-going pulses at the horizons, or by any noticeable change in noise levels, thus making its detection very difficult. We may term this kind of degradation "symmetrical optical degradation". (The rapid onset of asymmetrical degradation in channel 1 masked any initial symmetrical degradation.)

In the pages that follow we will present the culmination of our investigations to date in the form of nomograms showing *approximate corrections* due to apparent instrumental optical degradation to be applied to the equivalent blackbody temperature measurements, T_{BB}', from channels 1, 2, and 4, and to the effective radiant emittance measurements, $\overline{W}'$, from channels 3 and 5 of the TIROS III radiometer, as recorded on the Final Meteorological Radiation (FMR) Tapes and shown in maps and listings in the "TIROS III Radiation Data Catalog"[2]. It must be emphasized that *these corrections are only our best estimates based upon certain simplifying assumptions of the effects of a complicated degradation mechanism which we do not yet fully understand and that the measurements thus corrected may still contain appreciable uncertainties.*

Following the nomograms we will discuss in detail the investigations which revealed the symmetrical and asymmetrical optical degradation and describe the steps involved and the assumptions made in constructing the nomograms.

II. CORRECTION NOMOGRAMS

Nomograms for correcting the measured equivalent blackbody temperatures, T_{BB}', for the TIROS III infrared channels (channels 1, 2, and 4) and the measured effective radiant emittance values, $\overline{W}'$, for the short wave channels (channels 3 and 5) due to deg-

radation of the instrumental response are presented in Figs. 1-5 below. The theory and data utilized in the construction of these nomograms will be described in the rest of the report; in this section we shall only describe the use of the nomograms with the aid of a few examples.

As will be pointed out in the remainder of the text, two correction nomograms, one for each side of the radiometer, are needed for channel 1, since asymmetrical optical degradation appears to occur. Fig. 1a gives the corrections, δT_{BB}, which must be *added algebraically* to the measured channel 1 floor side values of T_{BB}' in order to account for the degradation of channel 1 with time. For example, if during orbit 115, an equivalent blackbody temperature $T_{BB}' = 226°K$ is observed through the floor side, applying the corresponding correction, $\delta T_{BB} = -6.6°K$, yields a final value of $T_{BB} = 226° + (-6.6°) = 219.4°K$.

Fig. 1b gives the corrections for the channel 1 wall side values of T_{BB}'. For example, if during orbit 115, an equivalent blackbody temperature $T_{BB}' = 210°K$ is observed through the wall side, applying the corresponding correction, $\delta T_{BB} = +9.4°K$, also yields a final value of $T_{BB} = 210° + (9.4°) = 219.4°K$.

Fig. 2 shows the correction nomogram for channel 2. In this case there is only one nomogram, valid for both sides, from which to obtain corrections to T_{BB}', since asymmetrical optical degradation does not appear to occur. For example, if during orbit 500 the measured equivalent blackbody temperature is $T_{BB}' = 260°K$ for either side, the correction is $\delta T_{BB} = +20.8°K$, and the corrected value becomes $T_{BB} = 260° + (20.8°) = 280.8°K$.

Fig. 3 shows the correction nomogram for channel 4, analogous to Fig. 2. For example, if during orbit 110, the observed equivalent blackbody temperature is $T_{BB}' = 270°K$ for either side, the correction is $\delta T_{BB} = +6.3°K$, and the corrected value becomes $T_{BB} = 270° + (6.3°) = 276.3°K$.

Figs. 4 and 5 give the factors, κ^i, as a function of orbit number, by which to *multiply* the measured values, $\overline{W}'$, for channels 3 and 5, to normalize the measurements to the data given by London.[3] Thus for orbit 100 the normalizing factors are 2.3 and 2.8, respectively, for channels 3 and 5. If a value of $\overline{W}' = 200$ watts m^{-2} is observed by channel 3, the normalized value becomes $\overline{W} = (2.3)(200) = 460$ watts m^{-2}. If a value of $\overline{W}' = 20$ watts m^{-2} is observed by channel 5, the normalized value becomes $\overline{W} = (2.8)(20) = 56$ watts m^{-2}.

III. SUMMARY OF INVESTIGATIONS INDICATING THE EARLY OCCURRENCE OF SYMMETRICAL OPTICAL DEGRADATION

TIROS radiometers flown to date have had no on-board calibration except the zero-reference space-viewed level, the observed shift of which is sufficient but not necessary to indicate that degradation in the response of the instrument has occurred.

In attempting to analyze the heat balance of the part of the globe viewed by the TIROS III radiation experiment (i.e., the "quasi-global" heat balance between N55° latitude and S55° latitude), inconsistencies appeared which indicated that the response characteristics of channels 2 and 4 (long wave radiation) and 3 and 5 (short wave radiation) had degraded after the last calibration of the radiometers. The only other explanation appeared to be the inconsistency that the Earth was absorbing more and more solar radiation and at the same time radiating less and less long wave radiation to space.

Figure 1a—Temperature correction, δT_{BB}, vs. orbit number, channel 1, floor side only. An equivalent blackbody temperature measurement, T_{BB}', should be corrected by adding algebraically the δT_{BB} value corresponding to the appropriate orbit number.

3

Figure 1b—Temperature correction, δT_{BB}, vs. orbit number, channel 1, wall side only. An equivalent blackbody temperature measurement, T_{BB}', should be corrected by adding algebraically the δT_{BB} value corresponding to the appropriate orbit number.

4

Figure 2.—Temperature correction, δT_{BB}, vs. orbit number, channel 2, both sides. An equivalent blackbody temperature measurement, $T_{BB}{'}$ should be corrected by adding the δT_{BB} value corresponding to the appropriate orbit number.
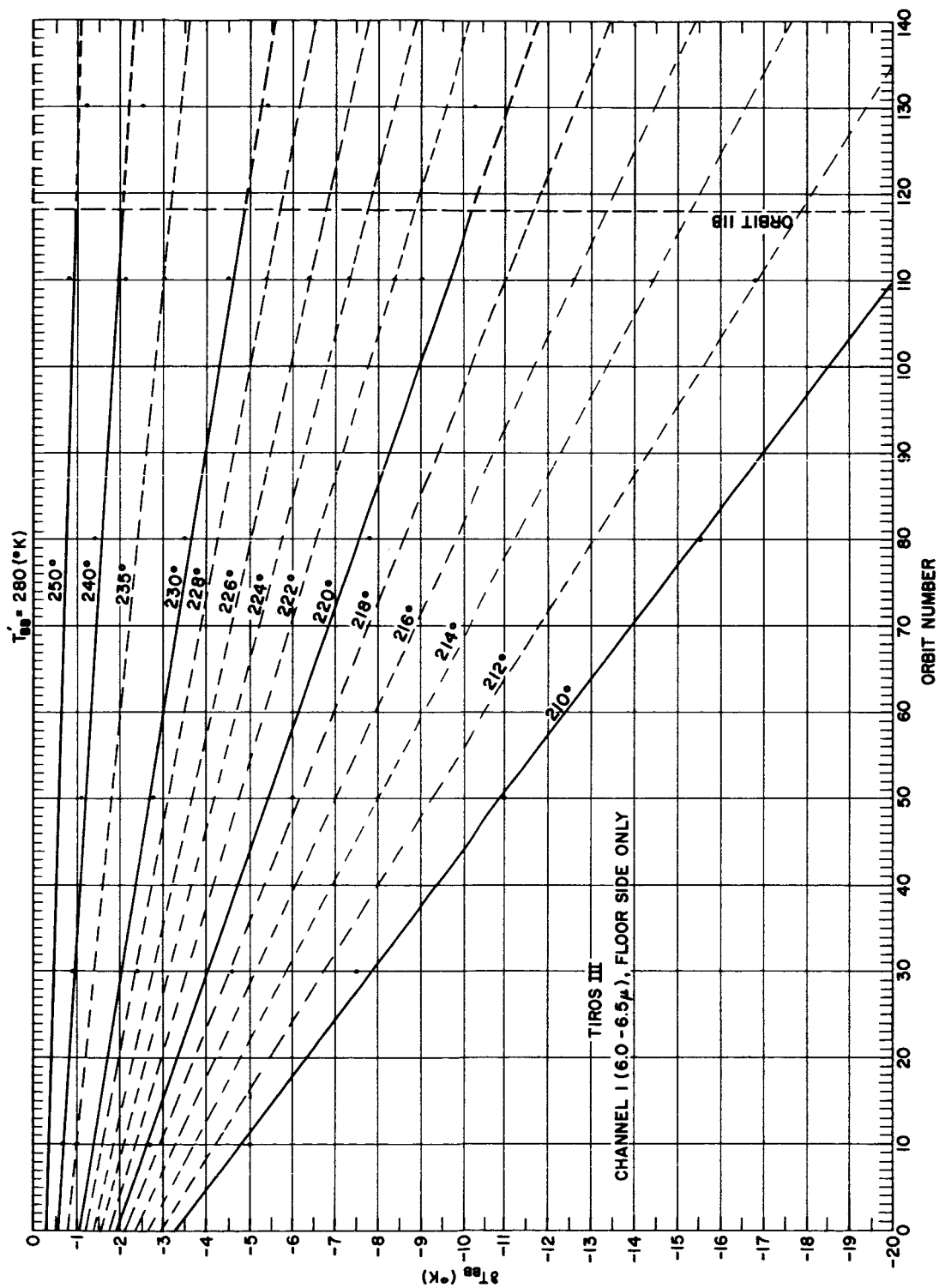
5

Figure 3—Temperature correction, δT_{BB}, vs. orbit number, channel 4, both sides. An equivalent blackbody temperature measurement, $T_{BB}{}'$, should be corrected by adding the δT_{BB} value corresponding to the appropriate orbit number.
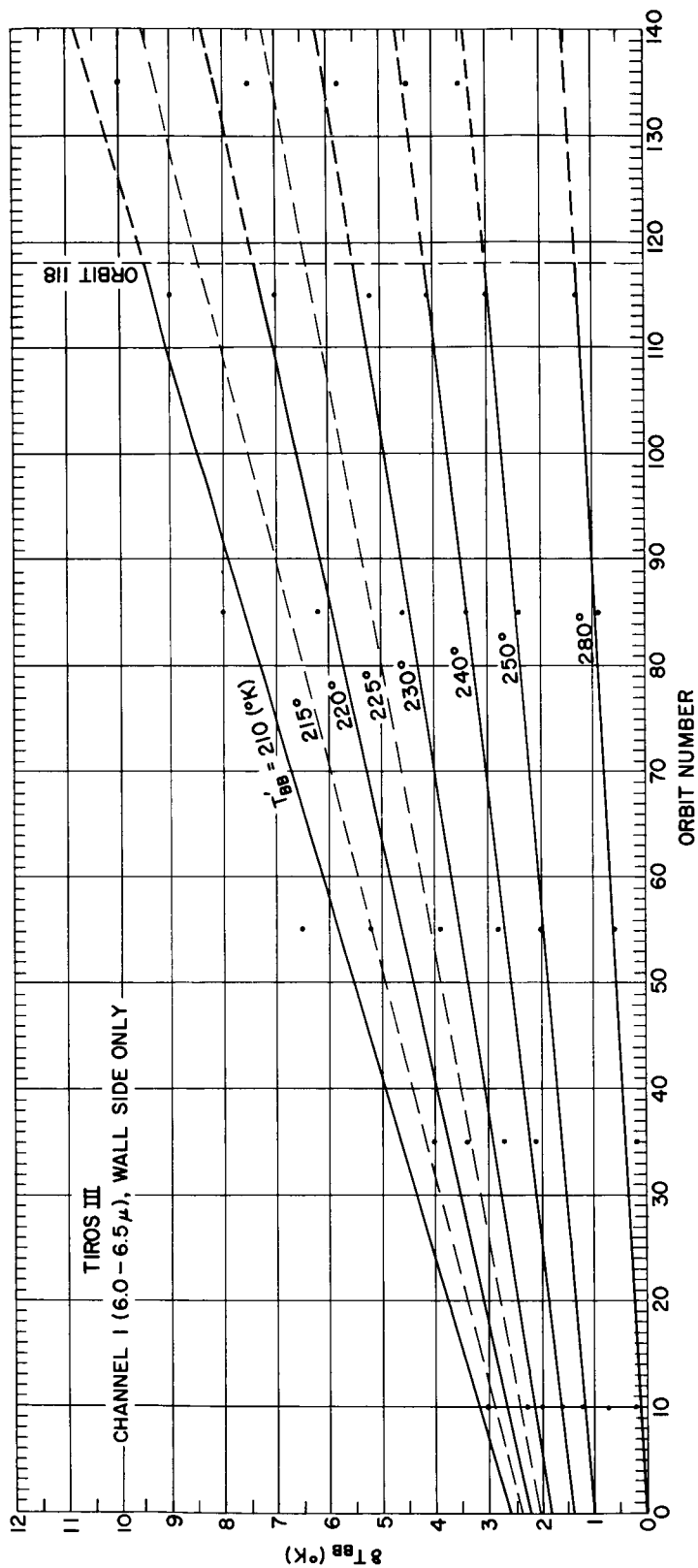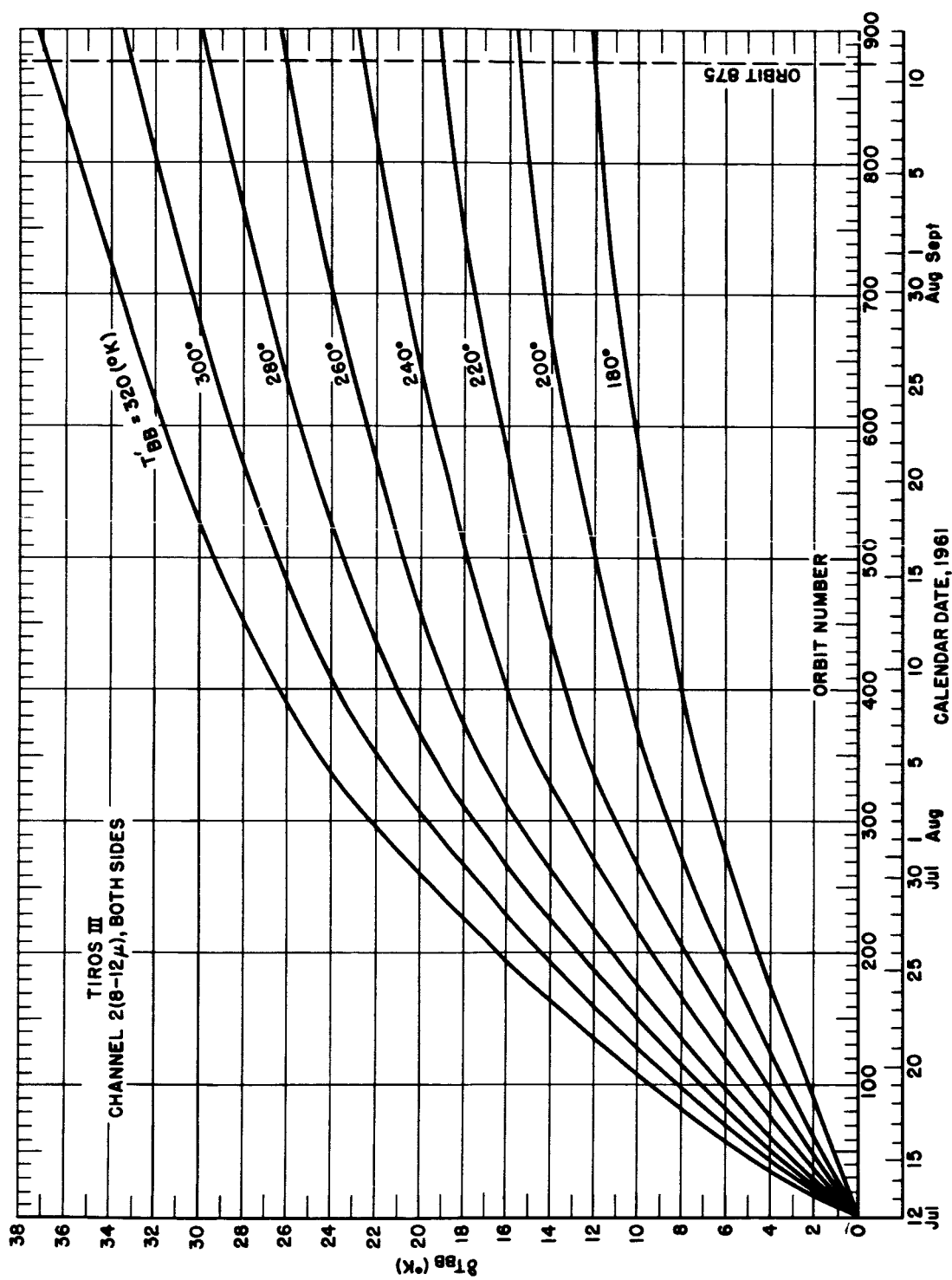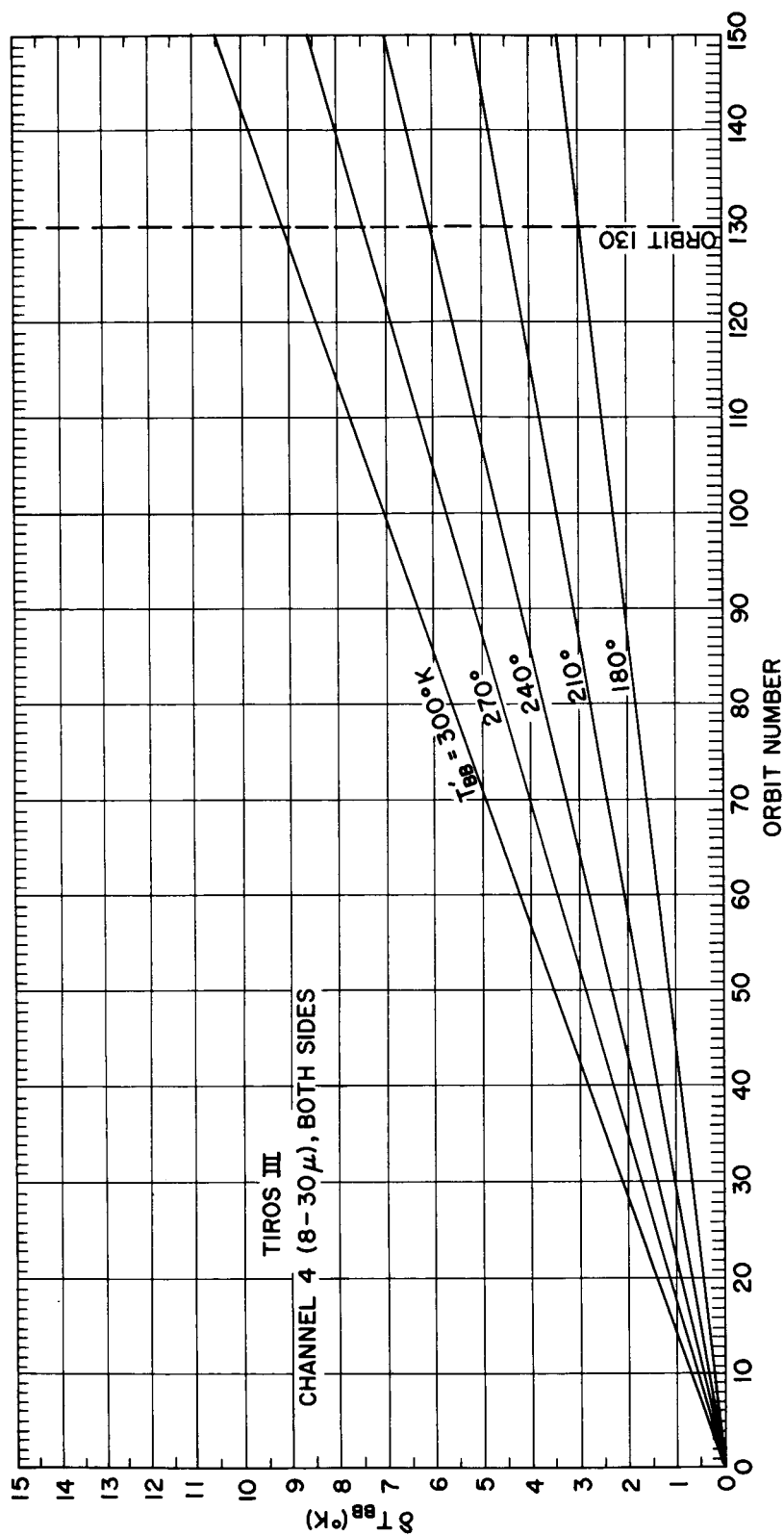
(private communication from Mr. J. Lienesch, U.S. Weather Bureau) indicating that the actual limb darkening is greater than the theoretically determined limb darkening for channels 2 and 4. The combined effect of these refinements would be to decrease our calculated outgoing long wave fluxes by about 3% for channel 2 and somewhat less for channel 4.

4.2 Method of Measuring Reflectance

Reflectances, r', from channel 3 and channel 5 data were calculated by

$$r' = \overline{W'}/\overline{W^*} \cos \theta_\circ \qquad (4.5)$$

where $\overline{W'}$ = measured effective radiant emittance
  $\overline{W^*}$ = effective solar constant
  $\theta_\circ$ = solar zenith angle

It was assumed that all solar radiation was diffusely reflected according to the Lambert Cosine Law and, hence, that reflectance and albedo were equivalent. Attempts have been made to develop an anisotropic backscattering function from measurements made by a five-channel radiometer, similar to the one carried on TIROS III, flown by the University of Michigan (under contract to NASA) on a high-altitude balloon. However, all such attempts to date have not affected the overall quasi-global albedos appreciably.

4.3 Description of the Multivariate Distribution Matrix

To determine the quasi-global heat balance using satellite data, one encounters a major problem in acquiring a truly representative distribution of measurements and in carrying out the numerical calculations to reflect accurately the spatial and temporal variations inherent in the data. Little can be done about the distribution of measurements from a single TIROS satellite. However, the numerical calculations can be designed to diminish the bias that exists in the data sample. The averaging of TIROS III radiation data over space and time was accomplished by an IBM 7090 computer program which places each measurement in a latitude-longitude compartment, spanning 10° of latitude and 15° of longitude. The range of latitudes is N55°-S55° and the range of longitudes is W0°-W360°. A latitude-longitude compartment is located in time by being placed in one of twenty-four hour compartments. Hence, there are eleven latitude intervals, twenty-four longitude intervals and twenty-four time intervals, making a total of 11 x 24 x 24 = 6336 latitude-longitude-hour compartments. This scheme is represented as a multivariate distribution matrix in Fig. 6.

4.4 Method of Averaging

For a specific latitude-longitude-hour compartment, a simple arithmetical average is taken of all measurements in the compartment. The circumglobal average in each 10° zone is obtained by giving equal weight to all compartments with an acceptable number of measurements, averaging first with respect to time and then with respect to longitude. This procedure may be expressed by the equation

$$\text{Zonal } ave = \frac{\displaystyle\sum_{k=1}^{d}\left\{\sum_{j=1}^{t}\left[\frac{\sum_{i=1}^{q} p_i}{q}\right]_j\Bigg/t\right\}_k}{d} \qquad (4.6)$$

11
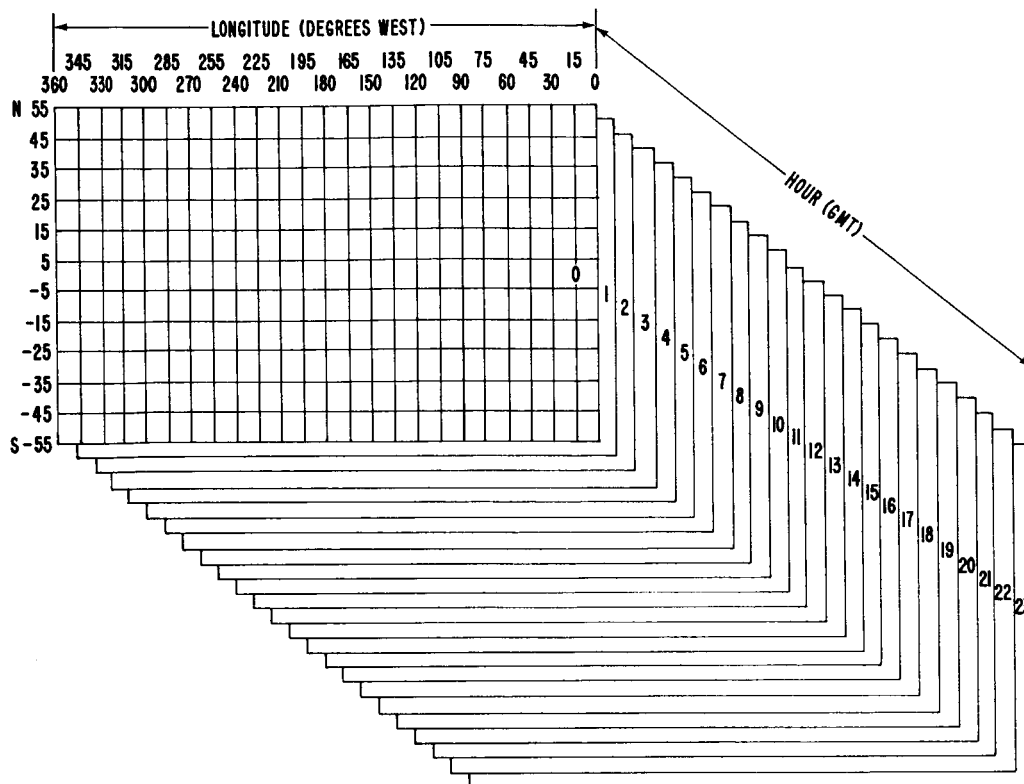
Figure 6—Schematic of the multivariate distribution matrix used in the "Heat Balance" program. Each small box represents a specific latitude-longitude-hour compartment.

where $p =$ an individual measurement of either total outgoing long wave radiant emittance or reflectance of solar radiation assigned to an applicable compartment

   $q =$ the number of individual measurements in a compartment

   $t =$ the number of compartments in the time dimension containing at least a specified minimum number of measurements, q_{min}, the latitude and longitude dimensions remaining constant. (The largest possible value of t is 24.)

   $d =$ the number of compartments containing acceptable time-averaged measurements in the longitude dimension, the latitude dimension remaining constant. (The largest possible value of d is 24.)

Cumulative zonal averages for TIROS III were developed over time periods of 44 and 27 days for channel 2, and 9 days for channels 3, 4, and 5. Intermediate cumulative averages (e.g., days 0-3, days 0-6, days 0-9, ...) were printed out approximately every three days and served the purpose of periodically ascertaining that the computer was carrying out its computations satisfactorily. The 9-day total period for channel 4 was determined by the termination of usable data. The 9-day intervals for channels 3 and 5 were established so that a mean declination of the sun could be used without introducing an appreciable error in the calculation of quasi-global albedos. The cumulative averages for channels

12

3 and 5 were obtained for eight 9-day periods, the accumulation of data being reinitiallized at the beginning of each succeeding period.

The 7090 "heat balance" program has the capability of specifying maximum or minimum limits for four parameters used in the calculations. These parametric limits are: (1) the maximum acceptable sensor nadir angle, η_{max}; (2) the maximum acceptable value for the minimum sensor nadir angle of each swath, NA_{test}; (3) the minimum number of measurements, q_{min}, to be accepted as representative for a latitude-longitude-hour compartment; and (4) the maximum acceptable solar zenith angle, $\theta_{\odot(max)}$. The maximum sensor nadir angle limit was imposed to eliminate "space contaminated" data (i.e., data from spots viewed partly on the earth and partly in space), NA_{test} was used to eliminate both closed and alternating modes, q_{min} was introduced to eliminate non-representative averages due to sparse data coverage, and $\theta_{\odot(max)}$ was used to assure that only reflectance measurements made in daylight were accepted from channels 3 and 5.

The limits used for the data from channels 2 and 4 were

$$\eta_{max} = 40°$$
$$NA_{test} = 26.4°$$
$$q_{min} = 7$$

and those for the data from channels 3 and 5 were

$$\eta_{max} = 40°$$
$$NA_{test} = 26.4°$$
$$q_{min} = 5$$
$$\theta_{\odot(max)} = 45°$$

In order to determine the quasi-global heat balance (between N55° and S55°), over a period of time, it was necessary to compare the cumulative quasi-global emitted radiant power, P^c, with the cumulative quasi-global albedo, A^c. The zonal averages of radiant emittance were multiplied by the zonal surface areas, and the resulting 11 products were summed to yield P^c, expressed mathematically by

$$P^c = 2\pi R_e^2 \sum_{i=1}^{11} (sin\ \zeta_2 - sin\ \zeta_1)_i\ W_{zonal\ ave\ (i)} \tag{4.7}$$

where R_e = radius of the earth (6,371,200 meters)
ζ_2 = northern zonal boundary latitude
$\zeta_1 = \zeta_2 - 10°$

In calculating A^c, use was made of the "zonal illuminated area cross section, Q", the projection on a plane normal to the sun's rays, of the zonal surface area lying on the illuminated side of the terminator (Fig. 7). The product of the solar constant and the value Q for a particular zone gives the total flux of solar radiation incident upon that zone at the top of the atmosphere. Each zonal albedo average was weighted, according to the ratio of its zonal illuminated area cross-section to the total illuminated area cross-section from which reflectance data were accepted, and these values were summed to yield A^c, expressed mathematically by

$$A^c = \frac{\sum_{i=1}^{n} \left[Q_i \times A_{zonal\ ave\ (i)} \right]}{\sum_{i=1}^{n} Q_i} \tag{4.8}$$
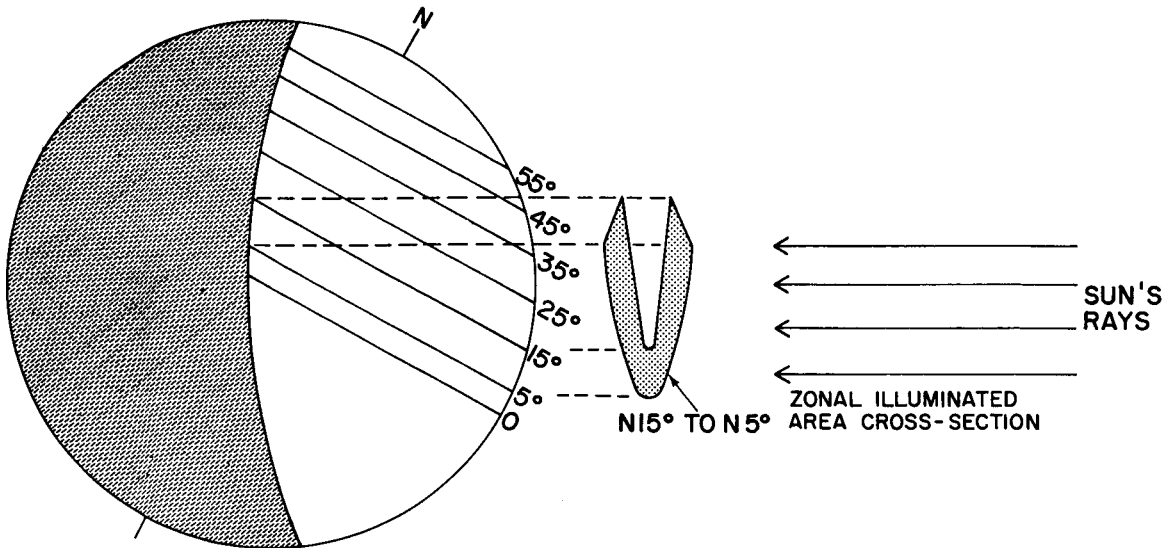
13

Figure 7—Representation of the "zonal illuminated area cross section, Q", used in calculating albedo. The zone N15° to N5° is illustrated.

where Q = zonal illuminated area cross-section

n = number of zones from which reflectance data were accepted

In Eq. (4.8) the number of zones from which reflectance data were accepted was generally less than 11 due to the combined constraints of the maximum acceptable solar zenith angle, the astronomical declination of the sun, and the orbit.

4.5 *Results of the Heat Balance Calculations*

Results of calculations of P^c from channels 2 (8-12μ) and 4 (8-30μ) and of A^c from channels 3 (0.2-6μ) and 5 (0.55-0.75μ) of TIROS III are shown in Fig. 8. Although Fig. 8 also illustrates similar results from channels 2 and 4 of TIROS II and channels 2, 3, and 5 of TIROS IV, only the TIROS III calculations will be discussed quantitatively in this Supplement. Similar evidence concerning sensor response degradation on subsequent TIROS satellites will be discussed in their respective Catalog-Manuals.

In Fig. 8 intermediate cumulative averages (e.g., days 0-3, days 0-6, days 0-9, etc.) were printed out approximately every three days by the computer as it developed each cumulative average. The intermediate values are indicated by the interconnected circled dots, and a final cumulative average is indicated by the final circled dot in each string of points. The initiation of a new cumulative average is indicated by a break in the interconnecting lines. Thus two separate sequences of cumulative averages for channel 2 of TIROS III, the first extending over a period of 44 days and the second over a period of 27 days (to orbit 875), are shown in Fig. 8. One cumulative average sequence for channel 4 over the first 9 days (to orbit 130, when evidence of asymmetrical optical degradation appeared) is shown in Fig. 8. It is seen that there is an apparent decrease of the cumulative quasi-global emitted radiant power calculated from both channels.

Values of the cumulative quasi-global emitted radiant power for the thermal radiation channels of TIROS II and IV also show decreases over the first several weeks but at somewhat lesser rates. For comparison, quasi-global emitted radiant power values were calculated from London[3] and are shown by arrows near the lower left-hand corner of Fig.

14
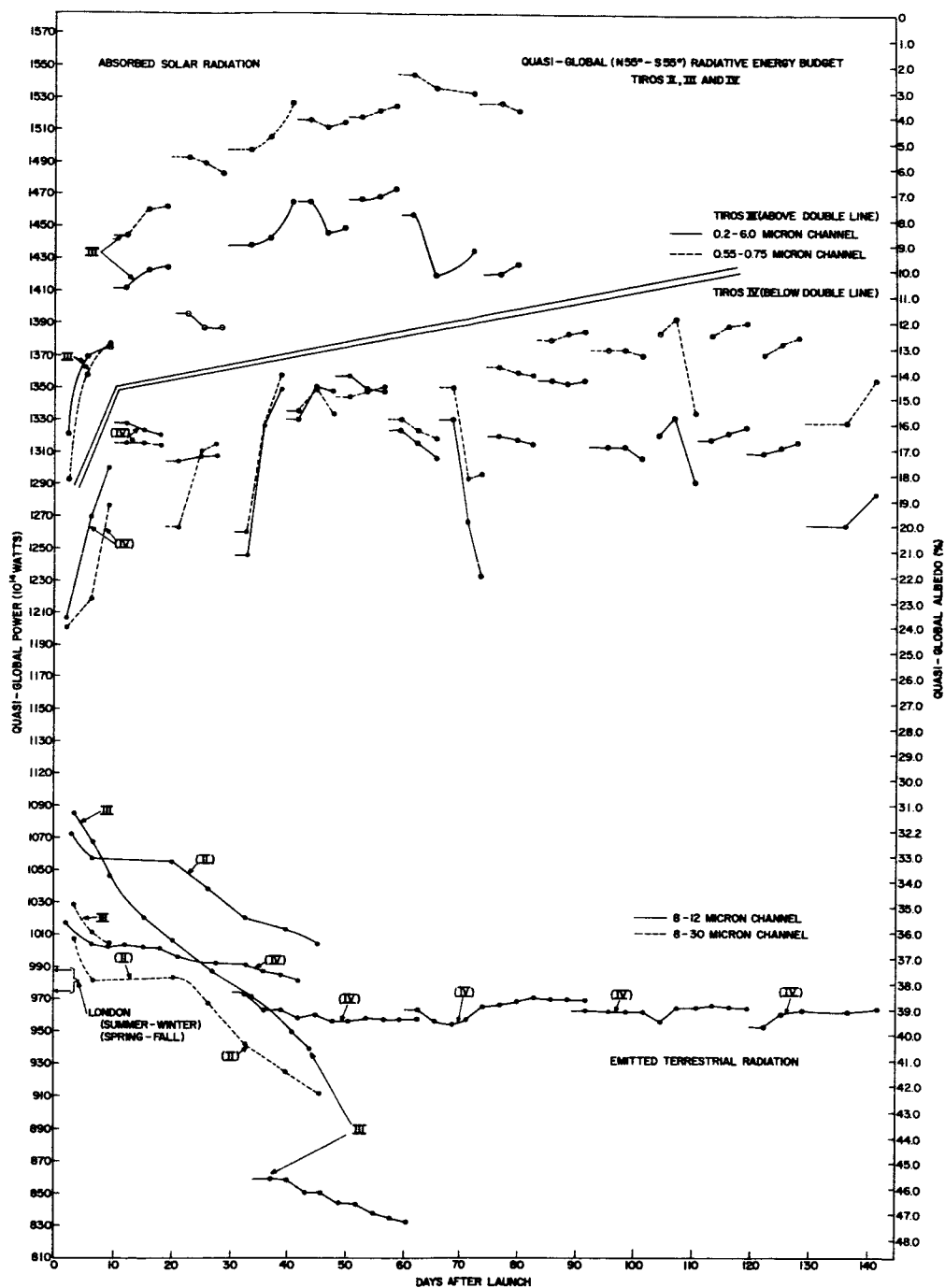
Figure 8—Quasi-global radiative energy budget, TIROS II, III, and IV. Quasi-global emitted radiant power along the left ordinate and quasi-global albedo along the right ordinate are plotted as a function of days after launch. Absorbed solar radiation [insolation over the quasi-globe x (1−albedo)] coincides with the left ordinate when averaged over all seasons. The large difference between absorbed solar radiation and emitted terrestrial radiation indicates a degradation of the instrumental response of all channels illustrated.

15

8. Because London investigated only the Northern Hemisphere, opposite seasons from 0° to N55° were combined as an approximation to represent the quasi-globe from N55° to S55°.

In treating data from the reflected solar radiation channels, the program calculated cumulative averages of quasi-global albedo, A^c, over successive periods of only 9 days. Thus, in Fig. 8, eight separate sequences of A^c for the reflected solar radiation channels of TIROS III are shown over a period of 80 days (to orbit 1152). The values of albedo along the right-hand ordinate are positioned such that the resulting annual absorbed solar radiation [insolation over the quasi-globe x (1 — albedo)] coincides with the ordinate on the left. Again it is seen that there is an apparent decrease with time of albedo with values from the 0.55-0.75μ channel decreasing more rapidly than those from the 0.2-6μ channel. It is difficult to interpret the reflected solar radiation results in light of the progressive decrease of the response of the 0.2-6μ channel observed before launch (see Section 6.1 of the Manual) and in light of the discrepancy existing between the comparative analysis of channels 3 and 5 shown in the Manual (Fig. 56) and the analysis of channels 3 and 5 shown in Fig. 8. From Fig. 8 the ratio of the channel 5 albedo to the channel 3 albedo shown in the initially plotted points (ending with orbit 33) is $(18.2/16.4) = 1.11$, whereas the corresponding ratio shown in Fig. 56 of the Manual is about 1.31. Furthermore, Fig. 8 indicates that the point in time when the albedos measured by the two channels are equal occurs in less than 10 days, whereas Fig. 56 of the Manual indicates that this event occurs at orbit 550 (or 38 days after launch). A partial explanation of the apparent discrepancy can be found in the ways in which the two analyses were carried out. Fig. 8 shows broad statistical averages of the entire range of measurements from the lowest to the highest reflectances. The ratios plotted in Fig. 56 of the Manual, on the other hand, were obtained from analog records where only relatively intense signals, presumably from overcast clouds, were analyzed. A scatter diagram of reflectances calculated from channel 3 and channel 5 data of TIROS III over Hurricane Anna on 21 July 1961 is shown in Fig. 9. This figure illustrates the skewed characteristic of the comparative reflectances calculated by means of Eq. (4.5) over a wide range of signal levels and qualitatively shows how the two analyses yielded different results. An investigation of the skewed characteristic is under way, considering such areas as the calibration procedure and the physical processes of scattering and absorption in the atmosphere, as well as instrumental degradation mechanisms. However, to date a satisfactory explanation of the skewed characteristic of Fig. 9 has not been found, consistent with the results from other satellite and balloon experiments, and we shall merely present it as an observation without speculation as to its cause. Further, it is difficult to reconcile the initial albedo measured by channel 5 (18.2% in Fig. 8) with the statement in the Manual that checks-of-calibration data did not indicate a decrease in the sensitivity of channel 5 before launch. There may have been a change between the last check of calibration on July 3 and launch on July 12, 1961, or perhaps factors present during launch or during the first few days of exposure to the space environment contribute to the apparently low initial values of A^c in Fig. 8.

Because of the angular motion of the spin vector of TIROS over the celestial sphere, occasionally the 45° half-angle conical figure, generated by the radiometer axis in the wall direction as the satellite spins, intersects the direct rays of the sun. Under these conditions, direct solar rays impinge upon the sensors from the wall direction momentarily, once during each satellite rotation. Such an unfavorable satellite-sun geometry may exist for one or two days until it is eliminated by a change in the attitude of the spacecraft. There were four periods in the history of TIROS III when such an unfavorable
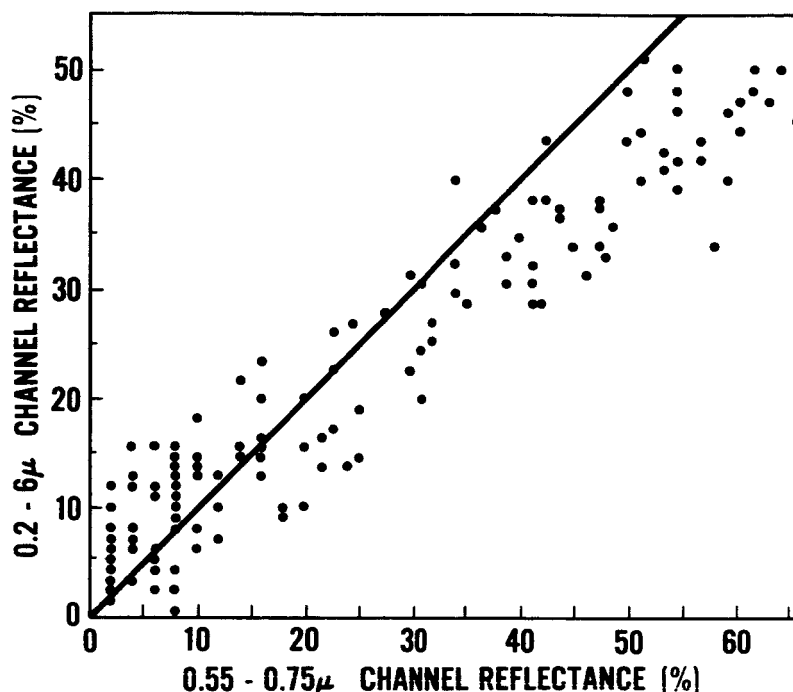
Figure 9— Scatter diagram illustrating the pronounced skewed characteristic of reflectances calculated from channels 3 (ordinate) and 5 (abscissa) of TIROS III. The data shown are not normalized and are from nine swaths over Hurricane Anna and adjacent ocean areas, orbit 132 R/0 133, 21 July 1961 (cf. p. 292, TIROS III Radiation Data Catalog[2]). The solid line is the locus of equal reflectances.

geometry occurred, viz., the periods including the orbits numbered 197-204 (Julian or TIROS III day 14), 296-300 (day 21), 452-471 (days 32-33), and 1061-1081 (days 74-75). The data from these orbits were not reduced and, hence, do not affect the plots shown in Fig. 8; nor is there any evidence in Fig. 8 that marginal contamination from the sun during the orbits immediately preceding or following these four intervals is present in the data.

In interpreting Fig. 8 it must be emphasized that radiative equilibrium can not be assumed for the quasi-globe; i.e., one can not equate absorbed solar radiation with emitted terrestrial radiation to yield the quasi-global heat balance. Heat is lost from the quasi-globe by other means than radiation, primarily through meridional wind and ocean current components crossing the N55° and S55° boundaries. Calculations from London's study[3] indicate that the annual quasi-global excess of absorbed solar radiation over emitted terrestrial radiation is 70×10^{14} watts.

Since no evidence of pre-launch degradation of the thermal channels of TIROS III (or any other TIROS satellite) has ever been detected, it is tempting to try to infer the quasi-global albedo by extrapolating the curves of the 8-12μ and 8-30μ channels back to the ordinate, keeping in mind the following two assumptions: (1) that the intercept value of total flux was correctly derived from satellite measurements, which at the time of launch were undegraded and represented accurately a quasi-global mean value, and (2) that 70×10^{14} watts represents the correct value of the quasi-global excess of absorbed solar radiation over emitted terrestrial radiation. From Fig. 8 the TIROS III 8-12μ

17

channel curve extrapolated backward in time intersects the ordinate at 1100 x 10¹⁴ watts. The quasi-global heat loss then becomes $(1100 + 70) \times 10^{14} = 1170 \times 10^{14}$ watts, and the albedo required to replenish 1170 x 10¹⁴ watts with absorbed solar radiation is 26.0%. (As suggested in Section 4.1, the channel 2 derived total outgoing fluxes may be about 3% too high. If this were true, the intersection would become $(1100/1.03) \times 10^{14} = 1068 \times 10^{14}$ watts. The quasi-global heat loss then becomes $(1068 + 70) \times 10^{14} = 1138 \times 10^{14}$ watts, and the corresponding quasi-global albedo becomes 28.0%.) The 8-30μ channel curve extrapolated backward intersects the ordinate at 1050 x 10¹⁴ watts. The quasi-global heat loss then becomes $(1050 + 70) \times 10^{14} = 1120 \times 10^{14}$ watts, and the corresponding quasi-global albedo becomes 29.1%. (Again, because of the reasons discussed in Section 4.1, the intersection of the 8-30μ channel curve may be slightly high.) However, all of these values are somewhat lower than the quasi-global annual albedo of 33.5% calculated from London's data[3].

The very rapid initial decrease of measured albedos implies that extrapolations back in time of the curves from the short wave channels would intersect the ordinate at albedo values comparable to those deduced above from the extrapolated thermal channel data. However, because of the lack of a sufficient and representative quantity of reflectance measurements in the first day or so when there is an apparent rapid change in the measurements and because of the history of prelaunch degradation, it appears impossible to extrapolate the albedo measurements back to the ordinate with any degree of confidence.

It is undoubtedly true that changing meteorological conditions contribute to short term fluctuations in P^c and A^c. Furthermore, the representativeness of the data is not without bias with regard to spatial and temporal distributions. However, it would appear extremely fortuitous if the earth were to radiate energy between latitudes N55° and S55° at a rate which steadily diminishes for a period of some weeks after every TIROS launch, while at the same time absorbing solar radiation at a rate which steadily increases, regardless of the season. The most plausible explanation appears to be that the response of the four radiometer channels of TIROS III, whose data are illustrated in Fig. 8, decreased during the time intervals shown. Thus, the primary purpose of the heat balance program has not been fulfilled due to the evidence of instrumental degradation which it revealed.[6]

V. CALCULATION OF THE QUASI-GLOBAL EMITTED RADIANT POWER, P^i

The philosophy that we have chosen to adopt is that on the average any decrease of P^c with time is due to degradation of the relevant radiometer channel. Once this statement is adopted as a working hypothesis we have a starting point for determining the degradation to attribute to a channel at any given time.

In order to calculate degradation models for channel 2 and channel 4, it is necessary to know the quasi-global emitted radiant power, P^i, between latitudes N55° and S55°, as a function of orbit number, i. In order to utilize the results of the long program used to determine P^c as described in Section IV, it was decided to obtain P^i from P^c rather than create another equally long program to determine P^i in the computer. We shall make use of the approximations listed below:

(1) All orbits which were used to obtain P^c will be weighted equally; i.e., it will be assumed that all orbits containing data contain an equal number of measurements, and that there is no bias to the magnitude of the data due to geographical location.

18

(2) The value of P^i corresponding to orbit i will be assumed to be the arithmetic average of P^{i-j} and P^{i+j} corresponding to orbits $(i-j)$ and $(i+j)$, respectively, where the number of orbits, j, is taken sufficiently large to contain a representative number of measurements and sufficiently small such that the degradation of the radiometer is approximately linear with time over the interval $(i-j)$ to $(i+j)$ orbits.

(3) It will be assumed that P^i is a smoothly varying function of orbit number, i, the variation (decrease) being due to degradation only.

Define m to be the number of orbits containing data used in determining P^c through orbit $(i-j)$, and n to be the number of orbits containing data used in determining P^c through orbit $(i+j)$, where j is an arbitrary number of orbits chosen so that approximation 2 above is satisfied. In practice we have found that $j \sim 25$ orbits is satisfactory.

It follows from the preceding discussion that the cumulative quasi-global emitted radiant power values for orbits $(i-j)$ and $(i+j)$ may be expressed respectively by

$$P^{c\,(i-j)} = \frac{1}{m} \sum_{1,2,\cdots m} P^* \tag{5.1}$$

and

$$P^{c\,(i+j)} = \frac{1}{n} \sum_{1,2,\cdots n} P^* = \frac{1}{n} \left[\sum_{1,2,\cdots m} P^* + \sum_{(m+1,\cdots n)} P^* \right] \tag{5.2}$$

where P^* is the quasi-global emitted radiant power for each of the orbits containing data which are included in the calculations of P^c. These orbits are identified by 1, 2, $\cdots (m)$, $(m+1)$, $(m+2)$, $\cdots n$. It follows from approximations (1) and (2) that

$$P^i = \frac{1}{n-m} \sum_{(m+1),\cdots n} P^* \tag{5.3}$$

Upon combining Eqs. (5.1), (5.2), and (5.3) we obtain the relation for P^i

$$P^i = \frac{1}{n-m} [nP^{c\,(i+j)} - mP^{c\,(i-j)}] \tag{5.4}$$

where P^i is now expressed in terms of known quantities.

A smooth curve is then fitted through a plot of the points of P^i vs. i as determined from Eq. (5.4). The curves for channels 2 and 4 are given in Fig. 10. No better method (e.g., a least squares fit) is used, since the inherent accuracy of any method depends upon the rather uncertain character of the given data. A rather subjective extrapolation of the curve to orbit zero is then performed. Since this zero-point extrapolation enters critically into our degradation models, a systematic error may be introduced at this point. The curve thus obtained is used to determine P^i for any given orbit number, i; approximation (3) above is inherent in any use of P^i thus determined in constructing degradation models.

VI. CALCULATION OF THE AVERAGE QUASI-GLOBAL EFFECTIVE RADIANT EMITTANCE, $\overline{W}_{ave}{}^i$

The average quasi-global radiant emittance, $W_{ave}{}^i$, is related to the quasi-global emitted radiant power, P^i, by

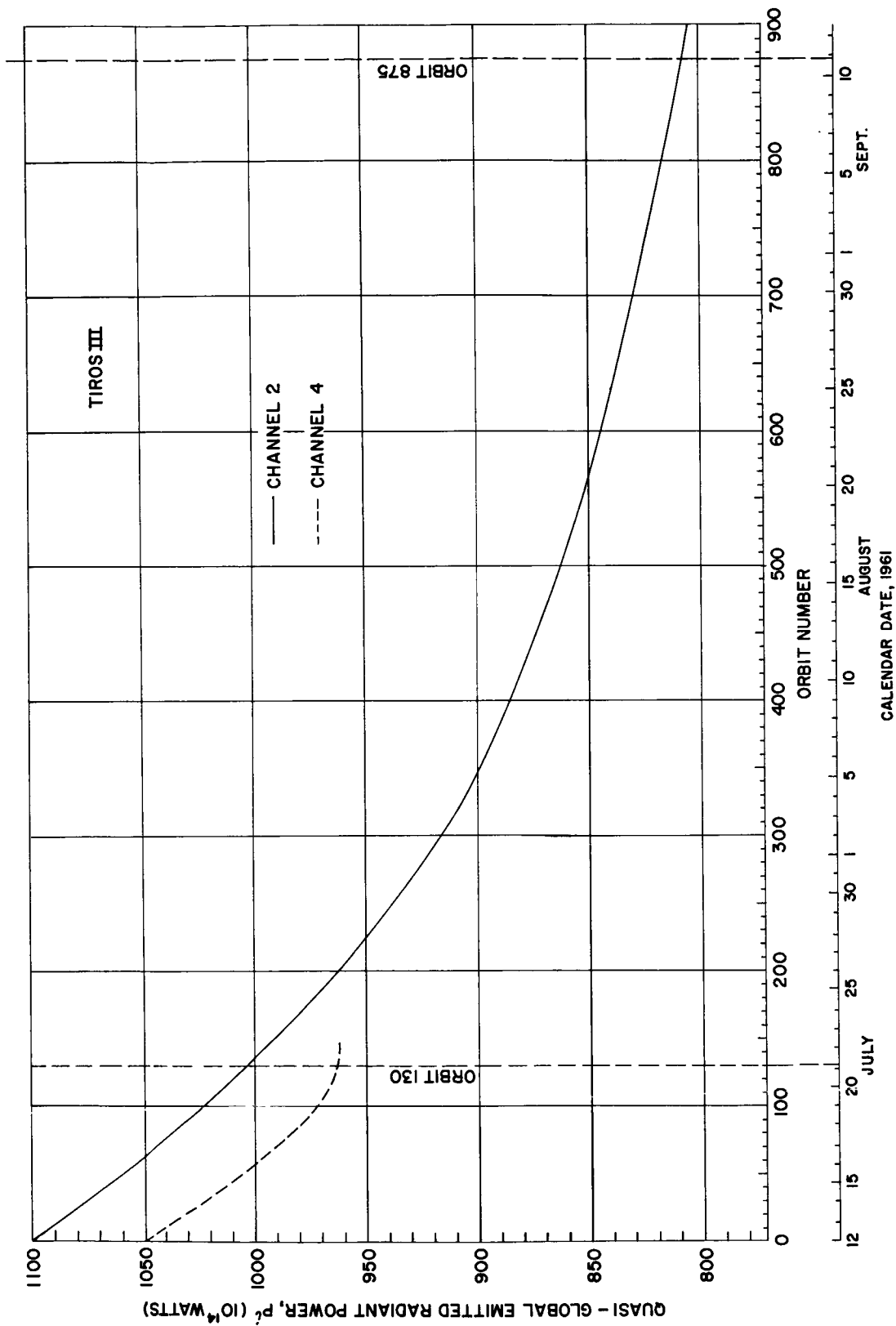$$W_{ave}{}^i = \frac{P^i}{4.1785 \times 10^{14}} \tag{6.1}$$

Figure 10—Quasi-global emitted radiant power, P^i, for channels 2 and 4 vs. orbit number. The data for channel 4 terminate with orbit 130 due to the onset of asymmetrical optical degradation.

where 4.1785 x 10¹⁴ meter² is the surface area of the earth between latitudes N55° and S55°.

In the development of degradation models, we shall require the relation between $\overline{W}_{ave}{}^i$ and $W_{ave}{}^i$. The relation is a rather complicated one, and is given by equations (4.1), (4.2), (4.3), (4.4). Now $\overline{W}_{ave}{}^i$ is an average over many values of the zenith angle, θ; we therefore seek an approximate relation between $\overline{W}_{ave}{}^i$ and $W_{ave}{}^i$ for some average value of θ. As indicated in Section IV, the maximum acceptable sensor nadir angle, η_{max}, was 40° for channels 2 and 4. The corresponding zenith angle at the surface of the Earth for a mean orbital height of 780 km is $\theta_{max} = 46.2°$.

Fig. 11 shows the relations between W and $\overline{W}$ for channels 2 and 4, calculated for zenith angles of 0°, 30°, and 46.2°. It is seen that the relationship is quite insensitive to the value of θ in the range 0° to 46.2°. Therefore, we have chosen the straight line approximations shown in Fig. 11, which are sufficiently accurate for our purpose.

It is assumed that quasi-global averages are related in the same way as individual measurements. Therefore, the linear equations derived from these curves are

$$W_{ave}{}^o = 3.63\,\overline{W}_{ave}{}^o + 92.5 \qquad\qquad \text{...Channel 2} \qquad\qquad (6.2)$$

and

$$W_{ave}{}^o = 2.19\,\overline{W}_{ave}{}^o + 30.0, \qquad\qquad \text{...Channel 4} \qquad\qquad (6.3)$$

where the superscript (°) refers to orbit zero when the radiometer measurements are assumed to be undegraded.

In the computer runs, the equations derived for the undegraded radiometer were used throughout. Hence, by definition, Eqs. (6.2) and (6.3) apply to any orbit i.

Finally, from Eqs. (6.1), (6.2), and (6.3), the quasi-global emitted radiant power derived from measurements is related to the average quasi-global effective radiant emittance at orbit i by

$$P^i = 4.1785 \times 10^{14}\,[r + s\,\overline{W}_{ave}{}^i] \qquad\qquad (6.4)$$

where for channel 2 ($s = 3.63;\ r = 92.5$), and for channel 4 ($s = 2.19;\ r = 30.0$). The constant s is dimensionless and r is in units of watts m^{-2}.

VII. INSTRUMENTAL RESPONSE DEGRADATION MODELS

7.1 *Optical Degradation*

Fig. 12 shows a block diagram of one channel of the medium resolution scanning radiometer[1,7]. The alternating voltage generated at the thermistor bolometer is proportional to the absolute difference in radiant flux absorbed by the bolometer between the chopper disc position shown in Fig. 12 and the diametrically opposite position of the chopper[7]. The letter W refers to radiant emittance, R is reflectivity, f is the transmittance of the lens-filter combination, α is the absorptivity of the bolometer, and ε is emissivity. Superscripts W and F refer to the wall and floor directions, b and m are the black and mirrored halves of the chopper, and s refers to radiation emitted from optical elements within the radiometer. Subscript p indicates the prism and c, the chopper.

21
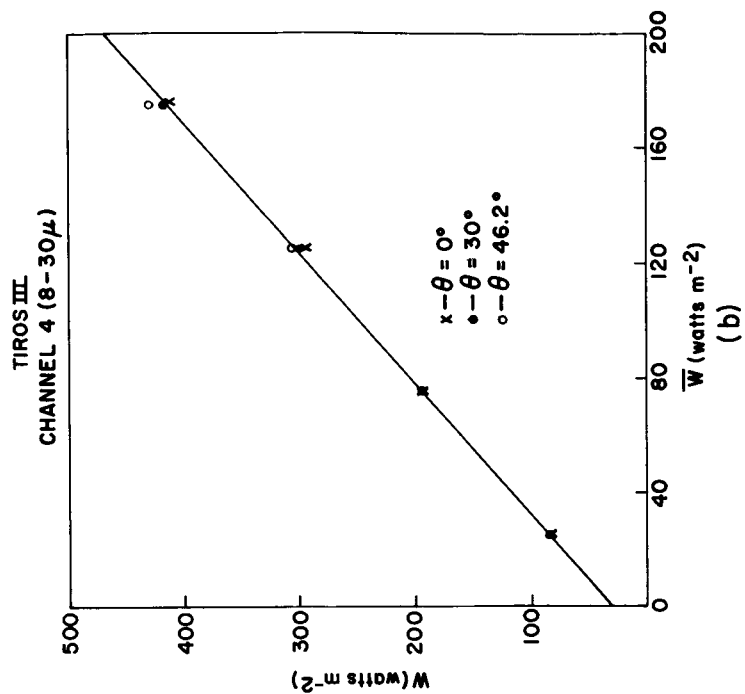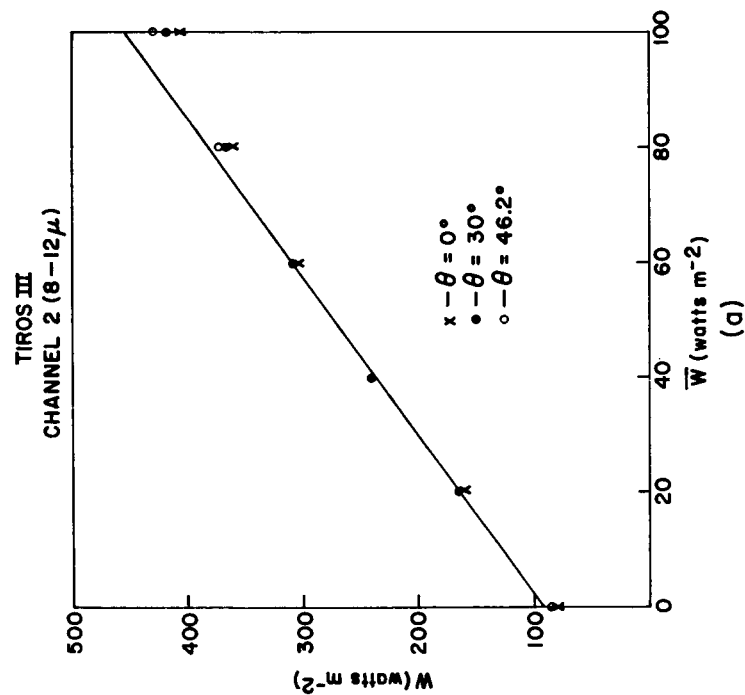
Figure 11—Total radiant emittance, W, plotted as a function of effective radiant emittance to which an undegraded sensor responds, $\overline{W}$, for channel 2 (a) and channel 4 (b) at zenith angles of 0°, 30° and 46.2°. The straight line approximations were adopted for further manipulation of the total flux values printed out by the computer.

22
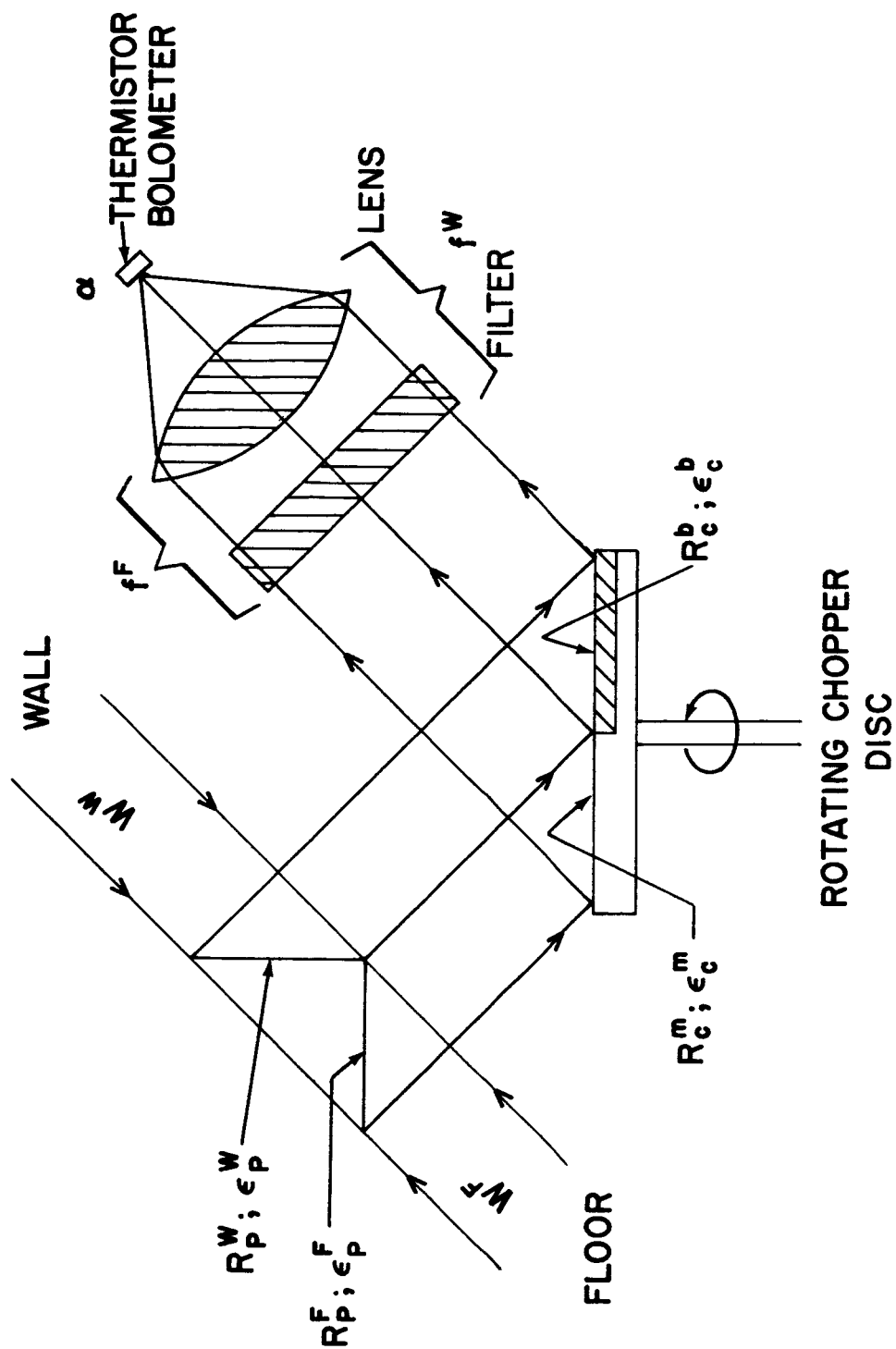
Figure 12—Block diagram of one channel of the medium resolution scanning radiometer [cf. Eq. (7.1)].

23

The bolometer absorbs radiation which originates within the field of view on the wall side, $W^W(\lambda)$, and the floor side, $W^F(\lambda)$, of the radiometer. The intensity and spectral distribution of the received radiation are modified by the reflecting surfaces of the prismatic mirror and of the chopper, but mainly by the transmission characteristics of filters and lenses (in an undegraded radiometer). Assuming that all optical elements in the system exist at the same temperature, each contributes to the radiation incident on the detector according to its own emissivity and the satellite interior temperature. Thus the radiant emittance from a given element can be expressed by $\varepsilon(\lambda)\ W^s(\lambda)$. In a properly balanced and aligned instrument the absolute difference in chopped radiant flux received by the bolometer becomes

$$\Delta\overline{W} = k_1 \mid \int_0^\infty \alpha\ [(W^W R_p{}^W R_c{}^b f^W + \varepsilon_p{}^W W^s R_c{}^b f^W + \varepsilon_c{}^b W^s f^W +$$
$$W^F R_p{}^F R_c{}^m f^F + \varepsilon_p{}^F W^s R_c{}^m f^F + \varepsilon_c{}^m W^s f^F) -$$
$$(W^W R_p{}^W R_c{}^m f^W + \varepsilon_p{}^W W^s R_c{}^m f^W + \varepsilon_c{}^m W^s f^W +$$
$$W^F R_p{}^F R_c{}^b f^F + \varepsilon_p{}^F W^s R_c{}^b f^F + \varepsilon_c{}^b W^s f^F)]\ d\lambda \mid \tag{7.1}$$

where k_1 is a constant of proportionality taking into account the geometric and optical characteristics of the instrument.

If we assume that Kirchhoff's law for an opaque surface is valid, viz.,

$$\varepsilon(\lambda) = 1 - R(\lambda) \tag{7.2}$$

Eq. (7.1) reduces, after some algebra, to

$$\Delta\overline{W} = k_1 \mid \int_0^\infty \alpha\ [W^F R_p{}^F (R_c{}^m - R_c{}^b) f^F -$$
$$W^W R_p{}^W (R_c{}^m - R_c{}^b) f^W +$$
$$R_p{}^W W^s (R_c{}^m - R_c{}^b) f^W -$$
$$R_p{}^F W^s (R_c{}^m - R_c{}^b) f^F]\ d\lambda \mid \tag{7.3}$$

Let us define effective response functions, $\phi^F(\lambda)$ and $\phi^W(\lambda)$, corresponding to the floor and wall paths of the optical system such that

$$\phi^F(\lambda) = \alpha\ R_p{}^F (R_c{}^m - R_c{}^b) f^F \tag{7.4}$$

and

$$\phi^W(\lambda) = \alpha\ R_p{}^W (R_c{}^m - R_c{}^b) f^W \tag{7.5}$$

With the aid of Eqs. (7.4) and (7.5), Eq. (7.3) reduces to

$$\Delta\overline{W} = k_1 \mid \int_0^\infty [W^F \phi^F - W^W \phi^W + W^s(\phi^W - \phi^F)]\ d\lambda \mid \tag{7.6}$$

In order to investigate degradation in the optical system we assume that

$$\phi^F(\lambda) = C^F \phi_\lambda{}^* \tag{7.7}$$

$$\phi^W(\lambda) = C^W \phi_\lambda{}^* \tag{7.8}$$

where $\phi_\lambda{}^*$ is the effective spectral response of the undegraded radiometer at the time of its calibration and C^F and C^W give the subsequent fractional degradation, respectively, for the floor and wall halves of the optical system. At the time of the calibration $C^F = C^W = 1$.

24

Note that C^F and C^W here are *assumed* to be independent of wavelength. In actuality these constants are probably wavelength-dependent. Substituting Eqs. (7.7) and (7.8) in (7.6) we have, for the difference in chopped radiant flux received by the bolometer in an instrument whose optical system may be degraded,

$$\Delta \overline{W} = k_1 \mid C^F \int_o^\infty W_\lambda{}^F \phi_\lambda{}^* d\lambda - C^W \int_o^\infty W_\lambda{}^W \phi_\lambda{}^* d\lambda + C^W \int_o^\infty W_\lambda{}^s \phi_\lambda{}^* d\lambda - C^F \int_o^\infty W_\lambda{}^s \phi_\lambda{}^* d\lambda \mid \quad (7.9)$$

From the relation [cf. Eq. (6) in the Manual]

$$\overline{W} = \int_o^\infty W_\lambda \phi_\lambda{}^* d\lambda \quad (7.10)$$

we finally obtain for Eq. (7.9) the result

$$\frac{\Delta \overline{W}}{k_1} = \overline{W}' = \mid C^F \overline{W}^F - C^W \overline{W}^W + (C^W - C^F) \overline{W}^s \mid \quad (7.11)$$

where $\overline{W}'$ is the value of effective radiant emittance of a viewed target which the radiometer sensor would actually measure in terms of the original calibration.

The alternating voltage generated at the thermistor bolometer is amplified and rectified, and the d.c. output voltage from the radiometer, V_{RAD}, is linearly proportional to the difference in radiant flux received by the detector. Thus from Eqs. (7.1) and (7.11)

$$V_{RAD} = k_2 \Delta \overline{W} = k \overline{W}' \quad (7.12)$$

where k_2 and k are constants of proportionality.

The calibration of the radiometer is carried out in terms of V_{RAD} which is processed further by electronics and telemetered to the ground[1]. Thus, when $C^F = C^W = 1$ and the wall direction views space ($\overline{W}^W = 0$) while a target fills the field of view in the floor direction, from Eqs. (7.11) and (7.12) the measured value and the actual value would be the same ($\overline{W}' = \overline{W}^F$). Any deviation from the equality $C^F = C^W = 1$ would, in general, cause the measured value to differ from the actual effective radiant emittance.

In order to better appreciate the information content of Eq. (7.11), we shall illustrate schematically several explicit degradation models as described below. The models to be considered, relevant for the thermal channels, are

1. $C^F = C^W < 1$ (symmetrical optical degradation)
2. $C^F < C^W = 1$ (asymmetrical optical degradation)
3. $C^F < C^W < 1$ (asymmetrical optical degradation)

Model I: Figure 13a is a plot in arbitrary units of $\overline{W}'$ vs. $\overline{W}^W$ and $\overline{W}^F$. The solid curve refers to the undegraded case, $C^F = C^W = 1$, and the dashed curve to the case $C^F = C^W = 0.75$. For $C^W = C^F = 1$ we note [cf. Eq. (7.11)] that as the radiometer scans the earth first from the floor side and then from the wall side the measured values of $\overline{W}'$ become, respectively,

$$\overline{W}' = \overline{W}^F$$

and $\quad (7.13)$

$$\overline{W}' = \overline{W}^W,$$

while the value of $\overline{W}'$ when both sides view outer space simultaneously (space-viewed level) is zero; i.e.,

Figure 13—Example of symmetrical optical degradation: (a) Measured values ($\overline{W}'$) vs. calibrated values for floor ($\overline{W}^F$) and wall ($\overline{W}^W$). The solid curves refer to the undegraded radiometer where $\overline{W}' = \overline{W}^F = \overline{W}^W$. The dashed curves refer to the degraded radiometer where $\overline{W}' < \overline{W}^F = \overline{W}^W$. (b) Schematic analog trace of an earth scan from the undegraded and degraded radiometer.

$$\overline{W}_{space}{}' = (1 - 1)\, \overline{W}^s = 0 \qquad (7.14)$$

Thus, the absolute value of the slope of the solid curve in Fig. 13a is unity, while the value of the space-viewed level corresponds to the calibrated space-viewed level.

In the case, $C^F = C^W = 0.75$, Eq. (7.11) becomes

$$\overline{W}' = 0.75\, \overline{W}^F$$

and $\qquad\qquad\qquad\qquad\qquad\qquad\qquad\qquad\qquad\qquad\qquad$ (7.15)

$$\overline{W}' = 0.75\, \overline{W}^W$$

for the floor and wall, respectively, while the space-viewed level remains the same as the calibrated space-viewed level. In this case the absolute value of the slope of the dashed curve in Fig. 13a is 0.75. Fig. 13b illustrates for these two cases hypothetical scans for the floor or wall.

Model II: This model refers to the case $C^F = 0.75$ and $C^W = 1.00$. We now obtain from Eq. (7.11) the expressions

$$\overline{W}' = |\, 0.75\, \overline{W}^F + 0.25\, \overline{W}^s\, |$$

and $\qquad\qquad\qquad\qquad\qquad\qquad\qquad\qquad\qquad\qquad\qquad$ (7.16)

$$\overline{W}' = |\, 1.00\, \overline{W}^W - 0.25\, \overline{W}^s\, |$$

for the values of $\overline{W}'$ obtained during an earth scan for the floor and wall sides, respectively. The expression for the space viewed level becomes

$$\overline{W}_{space}{}' = 0.25\, \overline{W}^s \qquad (7.17)$$

For the sake of a reasonable example, let us stipulate the relationship for the maximum effective radiant emittance (viz., when η is a minimum)

$$\overline{W}_{max}{}^F = \overline{W}_{max}{}^W = \overline{W}_{max} = (5\!/\!6)\, \overline{W}^s \qquad (7.18)$$

Eq. (7.16) then gives us for the measurements during a scan for the floor and wall sides, respectively,

$$\overline{W}_{max}{}' = 1.05\, \overline{W}_{max}{}^F$$

and $\qquad\qquad\qquad\qquad\qquad\qquad\qquad\qquad\qquad\qquad\qquad$ (7.19)

$$\overline{W}_{max}{}' = 0.70\, \overline{W}_{max}{}^W$$

and Eq. (7.17) gives us for the space-viewed level

$$\overline{W}_{space}{}' = 0.30\, \overline{W}_{max} \qquad (7.20)$$

Eqs. (7.16) through (7.20) are illustrated in Fig. 14a and 14b. The dashed curves of Fig. 14b are schematic scan patterns obtained through the wall and floor sides of the radiometer. In this example, the "negative going pulses" in the wall side scan are a necessary result of the finite field of view of the radiometer as it scans across the horizon. In Eq. (7.16) the term $\overline{W}^W$ refers to a target completely filling the 5° field of view of the radiometer. However, as the sensor's finite field-of-view traverses the horizons at the beginning and ending of a scan, a broad spectrum from zero upward of "space-contaminated values of $\overline{W}^W$" results. Eq. (7.16) shows that the measurement decreases to

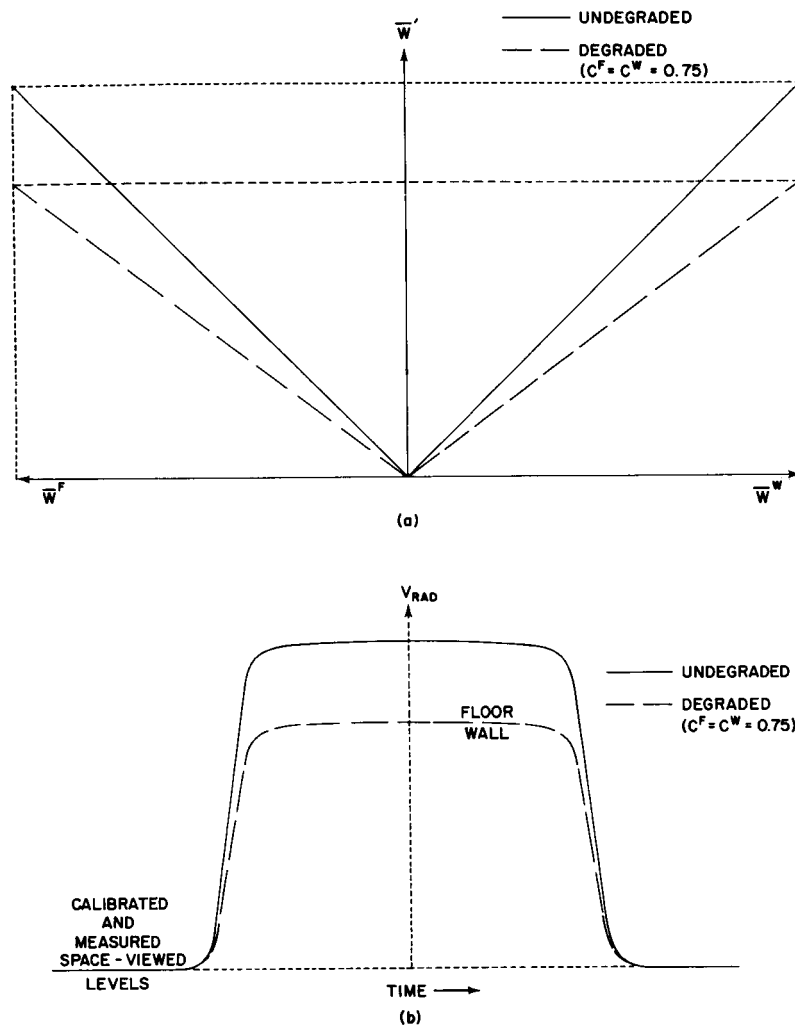*Figure 14*—Example of moderate asymmetrical optical degradation: (a) Measured values ($\overline{W}'$) vs. calibrated values for floor ($\overline{W}^F$) and wall ($\overline{W}^W$). The solid curves refer to the undegraded radiometer where $\overline{W}' = \overline{W}^F = \overline{W}^W$. The dashed curves refer to the degraded radiometer where $\overline{W}^F < \overline{W}' < \overline{W}^W$. (b) Schematic analog trace from the undegraded and degraded radiometer.

zero when the Earth fills the required fraction of the field-of-view such that

$$\text{``Space-contaminated } \overline{W}^w\text{''} = 0.25\ \overline{W}^s$$

Thus, the magnitude of the depth of the negative-going pulse should be precisely the difference between the measured and calibrated space-viewed levels, as illustrated in Fig. 14b. From Eq. (7.16) it can be seen that negative going pulses in the wall side scan could also result, even for an infinitesimal field-of-view, if at any point $\overline{W}^w$ were less than $0.50\ \overline{W}^s$. On the other hand, the floor side scan in this model can never include negative going pulses from the measured space-viewed level. Notice also that the maximum value of $\overline{W}'$ measured through the floor side exceeds the corresponding value which would have been measured by the undegraded radiometer.

Model III: The last model we shall consider is the more extreme one with $C^r = 0.20$ and $C^w = 0.70$. Eq. (7.11) now becomes

$$\overline{W}' = |\ 0.20\ \overline{W}^r + 0.50\ \overline{W}^s\ |$$

and
$$\overline{W}' = |\ 0.70\ \overline{W}^w - 0.50\ \overline{W}^s\ |,$$
$$\tag{7.21}$$

respectively, for the floor and wall earth scans, and the measured space-viewed level becomes

$$\overline{W}_{space}' = 0.50\ \overline{W}^s \tag{7.22}$$

If we now set

$$\overline{W}_{max}{}^F = \overline{W}_{max}{}^W = (\tfrac{2}{3})\ \overline{W}^s \tag{7.23}$$

in Eq. (7.21), reasonable values when high clouds are present, we obtain for the levels of the scans, respectively, for the floor and wall sides when the fields-of-view are completely filled

$$\overline{W}_{max}' = 0.95\ \overline{W}_{max}{}^F$$

and
$$\overline{W}_{min}' = 0.05\ \overline{W}_{max}{}^W$$
$$\tag{7.24}$$

The dashed curves in Fig. 15a follow from Eqs. (7.21) through (7.24), while Fig. 15b illustrates hypothetical scan traces for this model.

One can qualitatively reconstruct Fig. 15b either from Eq. (7.21) or from Fig. 15a. From Fig. 15a it is noted that the measured space viewed level, corresponding to $0.5\ \overline{W}^s$, is considerably higher than the calibrated space viewed level. Considering first the floor side (Fig. 15b), it is noted that as the radiometer field-of-view crosses the limb of the earth, and progresses across the earth's disk to the point nearest the satellite nadir, the value of $\overline{W}'$ increases to the value $\overline{W}_{max}'$ in Fig. 15a, but not nearly so rapidly as for the undegraded radiometer. As the field-of-view continues its journey across the earth's disk, the second half of the scan pattern is traced out. Conversely, as the wall side goes through the first half of any scan across the earth, the values of $\overline{W}'$ decrease down to a value $\overline{W}_{min}'$ which is only $0.033\ \overline{W}^s$ [cf. Eqs. (7.23) and (7.24)]. The magnitude of the rate of decrease for the wall side is 3.5 times the rate of increase for the floor side [cf. Eq. (7.21)], but only 0.7 times the rate of increase for either side of the undegraded radiometer. Note that the whole wall side scan has degenerated into one large "negative-
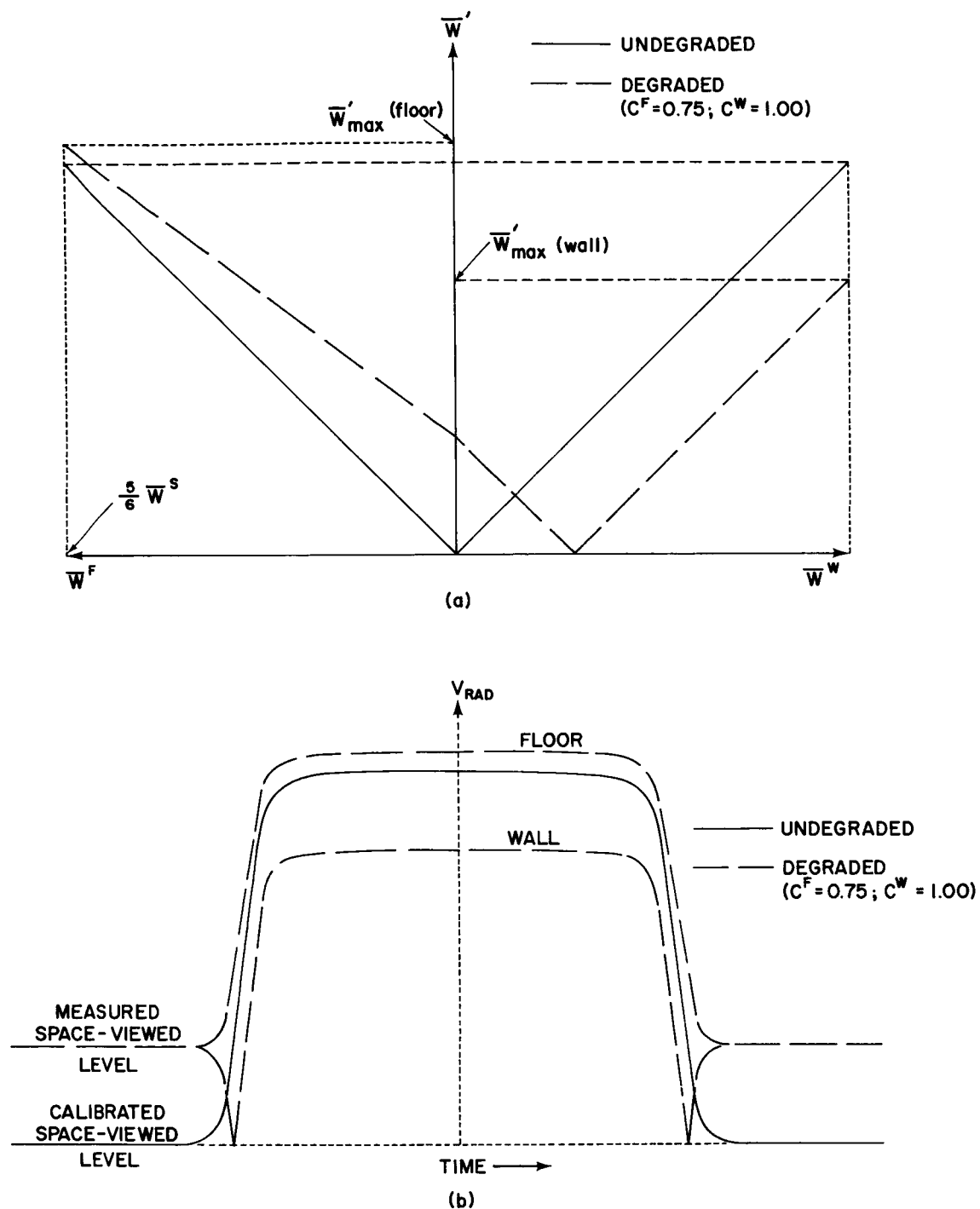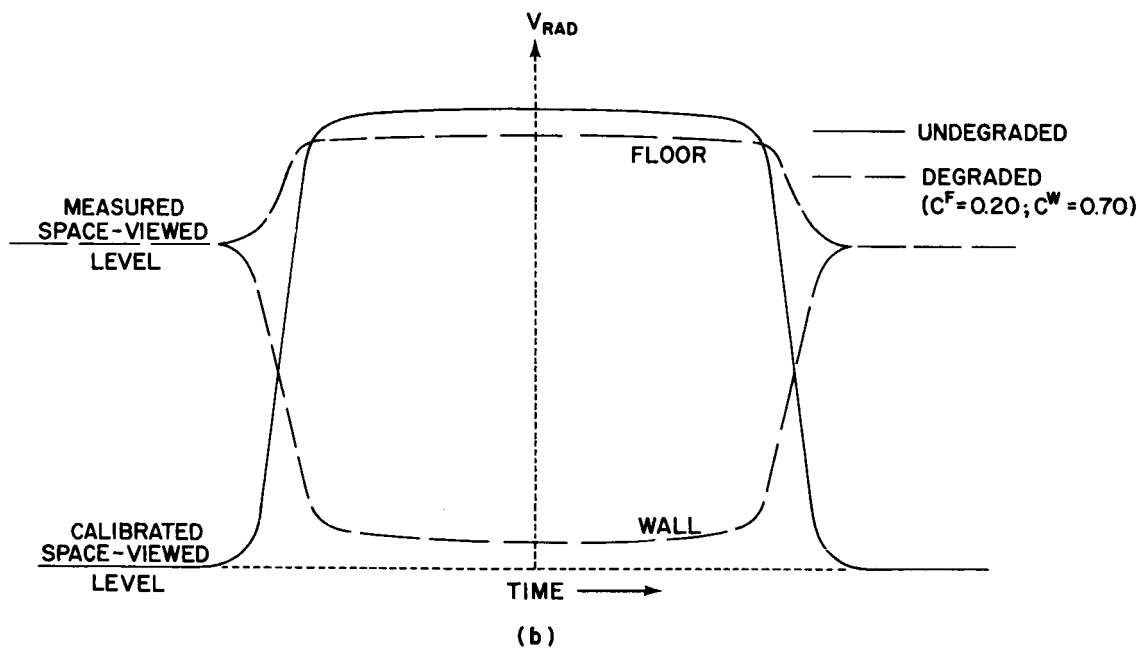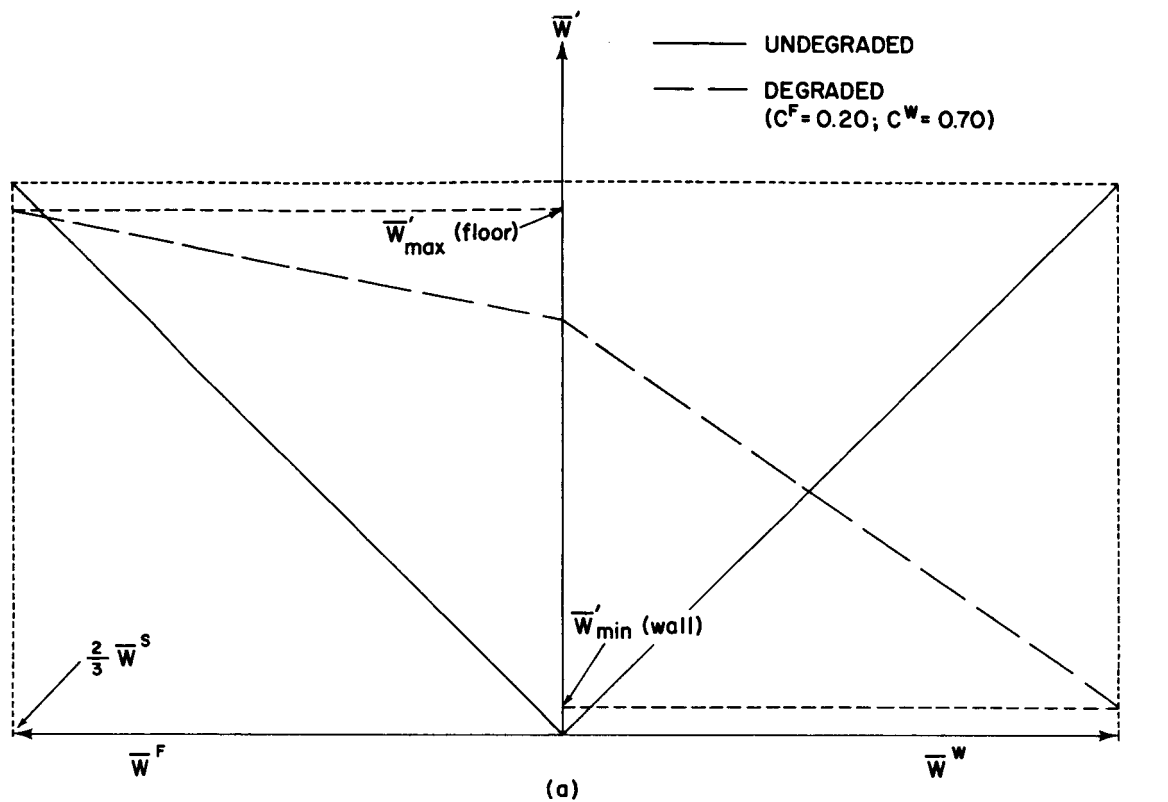
Figure 15—Example of extreme asymmetrical optical degradation: (a) Measured values ($\overline{W}'$) vs. cali-
brated values for floor ($\overline{W}^F$) and wall ($\overline{W}^W$). The solid curves refer to the undegraded radiometer
where $\overline{W}' = \overline{W}^F = \overline{W}^W$. The dashed curves refer to the degraded radiometer were $\overline{W}' < \overline{W}^F$
and $\overline{W}' \ll \overline{W}^W$. (b) Schematic analog trace from the undegraded and degraded radiometer.

30

going pulse" because of the extreme degradation of the floor side of the radiometer. Again the level of the floor side scan is always positive. This is precisely the effect found after several hundred orbits for both channel 1 and channel 4.

From Eq. (7.11) it is seen that the reflected solar radiation channels 3 and 5 would not show these negative-going pulses even if $C^r \neq C^w$, because $\overline{W}^s$ is essentially zero within the spectral response curves of these channels. This fact also implies that the space-viewed level should not depart from the calibrated space-viewed level due to optical degradation.

7.2 *Electronic Degradation*

The stability of the electronics employed in the various TIROS satellites is felt to be good—much better than the stability of the optical systems. This statement, of course, does not preclude the possibility that part of any degradation observed may be due to electronic instability, although the electronics remained very stable throughout the period of calibration before launch. In what follows we shall consider one component of the electronic system (voltage controlled oscillator) and describe in a qualitative manner how the data might be affected by electronic degradation. However, similar remarks could just as readily be directed at the electronic preamplifier contained in the radiometer housing. Because the ground demodulation equipment is readily accessible and constantly checked and aligned, the possibility of ground electronics persistently contributing to a degradation of the signal can be discounted.

Fig. 16a shows schematically the relationships between the voltage input, V_{RAD}, and the frequency output, F_{SC}, from the voltage controlled oscillator for a given electronics temperature, T_E (cf. Fig. 10 of the Manual). The solid curves refer to the calibrated relation; the dashed curves and the dash-dotted curves refer respectively to a translation and a rotation of the transfer function of the voltage controlled oscillator (VCO).

Since the same VCO is used for both sides, "symmetrical" electronic degradation will prevail in either case, in the sense that both sides of the radiometer will show the effect in exactly the same way. A translation will always result in a shift up or down in the observed space-viewed level, and a corresponding shift in the rest of the analog signal. The effect of a translation is schematically illustrated in Fig. 16b. The particular example of a rotation that we have picked results in no shift in the calibrated space-viewed level, since the dash-dotted curve in Fig. 16a coincides with the undegraded curve for $V_{RAD} = 0$. However, for all other values of V_{RAD} the output frequency, F_{SC}, is lower than it is in the undegraded case. The similarity between the effect of this rotation, which is schematically illustrated in Fig. 16b, and the example of symmetrical optical degradation in Fig. 13b points up the difficulty of distinguishing between the two from the limited diagnostic information at hand. It should be noted that we have illustrated only two of an infinite variety of possible electronic degradation models. In any event, electronic degradation of the VCO, as opposed to optical degradation, will *always* be characterized by a lack of negative-going pulses corresponding to scans across the horizon. Thus if a marked shift of the space-viewed level occurs, without the corresponding negative-going pulses at the beginning and end of each earth scan for *both* sides of the radiometer, we may conclude that electronic degradation rather than asymmetrical optical degradation is responsible. To date, no case of an appreciable translation in the VCO has been detected in any TIROS radiometer (including those on TIROS II and IV). Even when moderate asymmetrical optical degradation occurred in channels 1 and 4 of TIROS III, the lowest levels of the
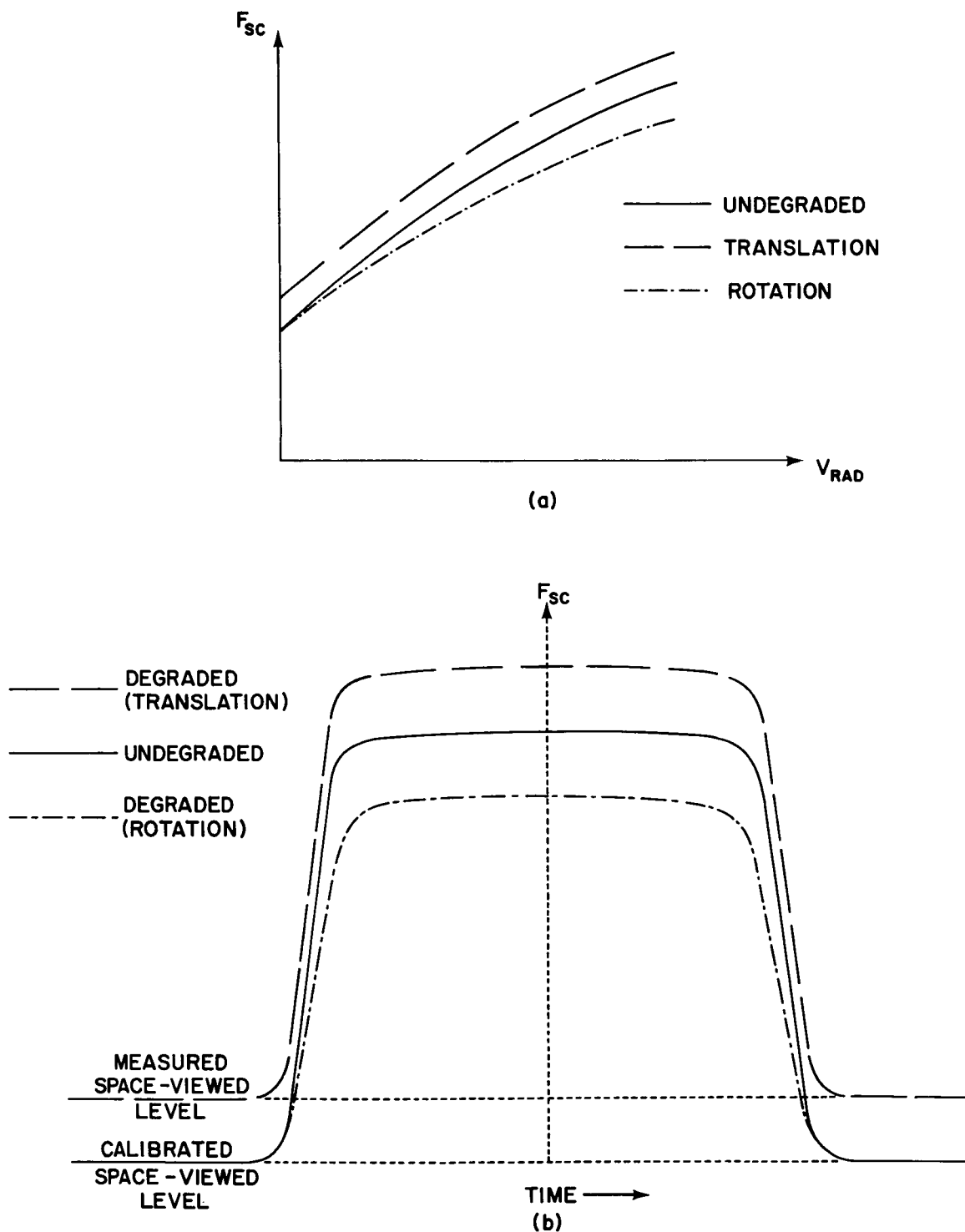
31

Figure 16—Example of electronic degradation of the voltage-controlled oscillator: (a) Output frequency, F_{SC}, vs. input voltage, V_{RAD}, for an undegraded oscillator and for a translation and a rotation of the transfer function. (b) Schematic analog traces corresponding to the three transfer functions in (a).

32

"negative-going pulses" coincided with the calibrated space-viewed levels, indicating that no shift in the VCO had compounded the effects due to optical degradation (cf. Fig. 14b). Similarly, the occurrence of a rotation of a VCO transfer function has never been established for any TIROS radiometer. It was pointed out that it would be difficult to distinguish between symmetrical optical degradation and a case of electronic degradation involving a rotation like that illustrated in Fig. 16b. However, the example of Fig. 16b is quite special and, in general, one would expect a rotation as well as a translation of the VCO transfer function to alter the space-viewed level (without the accompanying negative-going pulses characteristic of asymmetrical optical degradation). Since such characteristics have not been observed in any conclusive way in the radiation experiments flown to date, it seems reasonable to conclude that the primary degrading mechanism has been optical in nature.

Table I gives a summary of the discussions in this Section on instrumental response degradation. The rows refer to the type of degradation, and the columns to the observed effect. The word "yes" in the box corresponding to a given row and column indicates that the particular type of degradation referred to can cause the observed effect; "no" indicates that it cannot; and "maybe" indicates that it may or may not.

The table is only qualitative and should be used with caution. For example, the radiometer is in general slightly out of balance due to imperfect optical alignment at the time of calibration. This is illustrated graphically on pages 29-58 of the Manual. Asymmetrical optical degradation in the right direction could conceivably have the effect of balancing the radiometer, with a subsequent lowering of the observed space-viewed level in the case of the infrared channels. Other slight modifications of the table can occur under certain circumstances that are not germane to the scope of this Supplement.

VIII. CORRECTION MODELS FOR INFRARED RADIATION CHANNELS

All correction models for the infrared channels will be based on the assumption that only optical degradation prevails, since the electronics of the radiometers are believed to be quite stable.

8.1 *Channel 1*

Three observations pertinent to optical degradation of channel 1 were noted:

(1) The observed space-viewed level corresponding to a given housing temperature, T_c, is greater on launch day than the calibrated space viewed level, and thereafter increases in an accelerated fashion with increasing orbit number. Fig. 17 graphically illustrates the difference between the calibrated and space viewed levels as determined from a computer diagnostic. The values thus determined agree well with spot checks obtained from various analog records.

(2) A negative-going pulse relative to the observed space-viewed level is found to exist at both horizons of a scan across the earth through the wall side of the radiometer. In practice, this is very difficult to discern until appreciable degradation has already occurred (after orbit 118), due to the inherently noisy character of the channel 1 signal.

(3) Consistently lower radiant emittance values are measured through the wall side of the channel 1 radiometer than through the floor side.
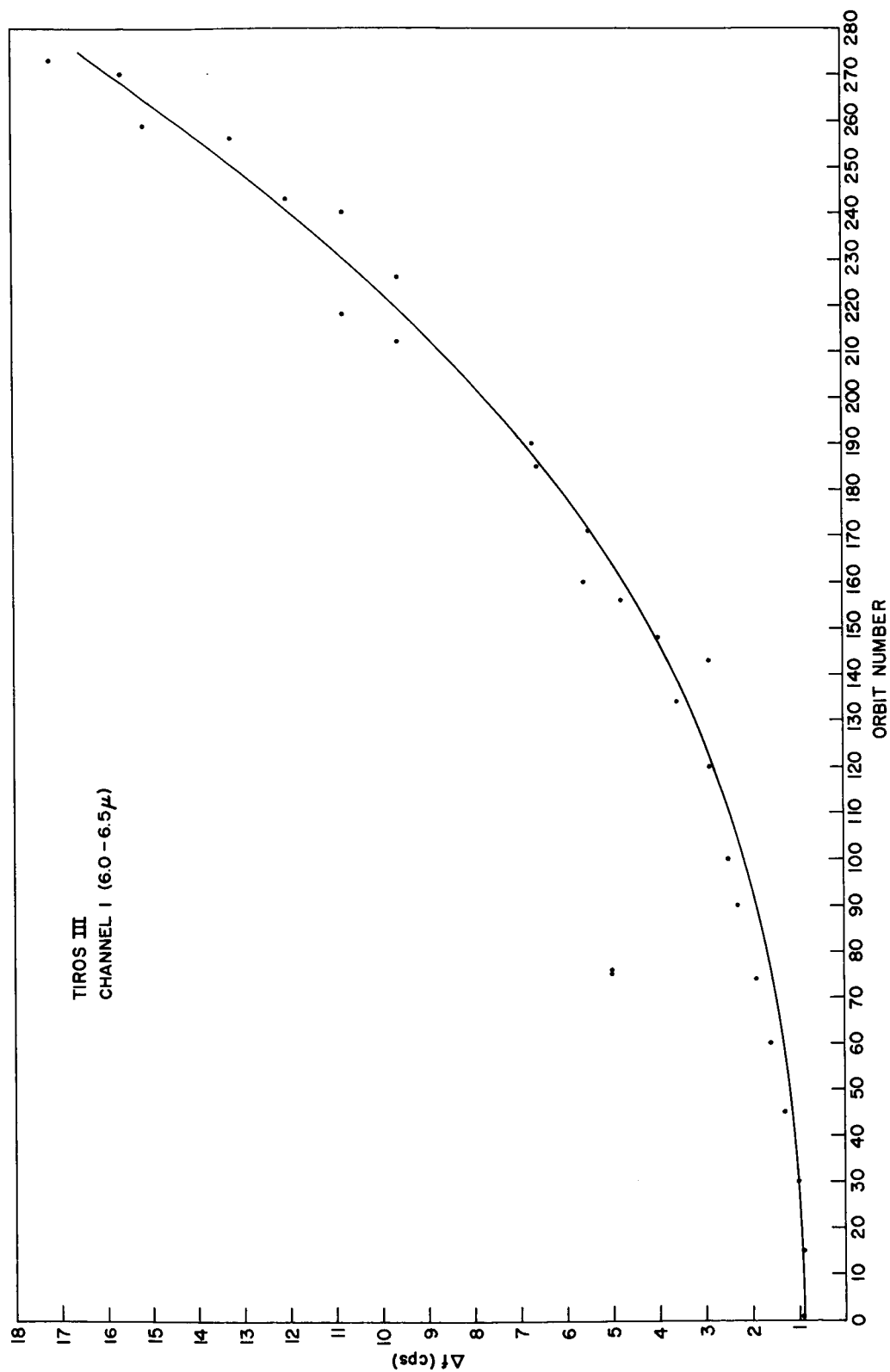
33

Figure 17—Difference (Δf) in cycles per second between the flight measured and the ground calibrated space-viewed levels as a function of orbit number for TIROS III, channel 1.

34

TABLE I

Types of Degradation vs. Their Observed Effects

......CAUSE THESE OBSERVED EFFECTS?

CAN THESE TYPES OF DEGRADATION......		Change of response of radiometer relative to observed space-viewed level	Shift of Space-viewed level		Appearance of negative-going pulses at each horizon		Relative change of response between wall and floor
			UP	DOWN	Thermal Channels	Solar Channels	
Optical	Symmetrical	Yes	No	No	No	No	No
Optical	Asymmetrical	Yes	Yes	No	Yes*	No	Yes
Electronic	Translational (in Freq.)	No	Yes	Yes	No	No	No
Electronic	Rotational	Yes	Maybe	Maybe	No	No	No

*Can occur on either the wall or the floor side, but not both.

35

All three of these facts point to asymmetrical optical degradation as outlined in Section VII (cf. Table I). According to this model the effective radiant emittance, $\overline{W}'^{(i)}$, measured on orbit i over any geographical location may be expressed by [cf. Sect. VII, Eq. (7.11)]

$$\overline{W}'^{(i)} = \mid C^{F(i)} \overline{W}^F - C^{W(i)} \overline{W}^W + (C^{W(i)} - C^{F(i)}) \overline{W}^{S(i)} \mid \tag{8.1}$$

where $C^{F(i)}$ and $C^{W(i)}$ refer respectively to the percentage degradation suffered by the floor and wall sides of the radiometer by orbit i. $\overline{W}^F$ and $\overline{W}^W$ are the respective effective radiant emittances which would have been observed with the undegraded radiometer. $\overline{W}^{S(i)}$ is the effective radiant emittance which corresponds to the average housing temperature on orbit i, a quantity which shows little diurnal variation.

When both sides of the radiometer are viewing outer space simultaneously, the observed space-viewed level is

$$\overline{W}_{space}'^{(i)} = \mid C^{W(i)} - C^{F(i)} \mid \overline{W}^{S(i)} \tag{8.2}$$

In our approximate scheme the calibrated space-viewed level is taken to be identically zero; thus from Eq. (8.2) any increase of the observed space-viewed level over the calibrated space viewed level gives a direct means of determining the difference in degradation of one side of the radiometer relative to the other. In practice there will, in general, be a small imbalance of the radiometer at the time of calibration. In what follows we shall ignore this small imbalance.

It would be highly desirable to have another relationship which is readily determinable between $C^{W(i)}$ and $C^{F(i)}$, in addition to Eq. (8.2). For example, if the outgoing effective radiance in the direction of the satellite from a given viewed spot could be calculated accurately as of the time of the measurement, the resulting known values of $\overline{W}^F$ and $\overline{W}^W$ (where, in terms of the calibration, $\overline{W} = \pi \overline{N}$) would uniquely permit the determination of $C^{W(i)}$ and $C^{F(i)}$ from Eqs. (8.1) and (8.2). However, such calculations are rather tedious, involving a detailed knowledge of the structure of the atmosphere (e.g., distributions of temperature, pressure, water vapor, and particulate matter) for the solution of the radiative transfer problem, and the results often contain uncertainties larger than the accuracy required for the determination of the degradation constants. Thus, in practice, only Eq. (8.2) remains for us to use.

The analog records indicate that the floor side of the radiometer degrades much more rapidly than the wall side. It seems significant to point out that generally the floor side (in the direction of the television cameras) is exposed to the daytime half of.the earth, whereas the wall side is exposed to the nighttime half. Thus, if reflected visible and ultraviolet radiation causes a deterioration of the optical elements, the deterioration would tend to be more pronounced on the floor side of the radiometer.

In view of the foregoing discussion it was decided that to a first approximation the wall half side of the radiometer could be considered undegraded through orbit 118, i.e., $C^W = 1$. The procedure for constructing the correction nomograms as given in Figs. 1a and 1b then consists of the following steps:

a) Determine the difference Δf in cycles per second between the calibrated and space-viewed levels for a given orbit i from Fig. 17. In constructing the correction nomogram this was done for every tenth orbit through orbit 150.

b) Determine the equivalent blackbody temperature, T_{BB}, corresponding to this frequency difference Δf from Figs. 17-22 of the Manual for a known housing temperature, T_C.

36

optical degradation model was considered to be appropriate. The procedure for constructing the correction nomogram parallels exactly the one for channel 2.

From Eq. (6.4) we obtain the relation for channel 4

$$\overline{W}_{ave}{}^i = \frac{P^i}{9.1509 \times 10^{14}} - 13.699 \qquad (8.8)$$

Combining Eq. (8.6) and Eq. (8.8) we obtain

$$\overline{W}'^{(i)} = \overline{W}\,\frac{P^i - 125.358 \times 10^{14}}{P^o - 125.358 \times 10^{14}} \qquad (8.9)$$

The construction of the correction nomogram for channel 4 in Fig. 3 paralleled exactly the construction of that for channel 2, except that P^i was determined for every 30 orbits instead of every 50, and the range of i was constrained to $0 \leq i \leq 150$ orbits. The estimated absolute accuracy given in the Manual is revised to read $\pm 4°$ to $\pm 8°K$ up to orbit 130 after applying corrections from Fig. 3.

8.4 *Case Studies of Channels 2 and 4*

In order to test the validity of the corrections for channels 2 and 4, eight case studies of synoptic situations were made. The geographical locations of these eight cases were picked on the basis of wide-spread clear sky conditions indicated by both TIROS III photographs and ground station and ship reports. In general all sea surface temperatures were estimated to be equal to measured bucket temperatures obtained from ships in the area. When data were not available for sea level shelter temperatures, these temperatures were estimated to be equal to the measured bucket temperatures. Surface temperatures for the plains region of the United States at about midday were estimated to be $5°K$ warmer than the corresponding shelter temperatures. Surface temperatures of the Sahara were taken to be in the range $10°K$-$25°K$ warmer than the corresponding shelter temperature. In all cases the emissivity of the surface was taken to be unity.

Radiosonde data were utilized to obtain pressure and temperature profiles and corresponding water vapor mixing ratios in the lower atmosphere up to about 300 mb. Above this level pressure and temperature profiles were adopted, based on rocket grenade experiments conducted at Wallops Island, Virginia, on 13 and 14 July, and 16 September, 1961[8], or, for orbits 43 and 117, based on the ARDC Standard Atmosphere (1959). Water vapor mixing ratios between 300 mb and 100 mb were taken to be saturated with respect to ice. Above 100 mb, constant mixing ratios were adopted. The top of the atmosphere was taken to correspond to a pressure of 0.1 mb.

An ozone distribution based on a 3 year mean of measurements made at Arosa, Switzerland[9] was utilized in constructing model atmospheres in connection with orbits 43 and 117. An ozone distribution based on work by Tønsberg and Olsen, given in Manabe and Möller,[10] normalized to a total ozone content of .290 cm/NTP as determined from ozone measurements at various U.S. and Canadian stations during the last two weeks of August 1961, was utilized in constructing model atmospheres corresponding to the other six cases studied. The computer program used to calculate the intensity of outgoing radiation for a particular model atmosphere is the one described by Wark, Yamamato, and Lienesch.[4]

Table II gives a summary of the results. Columns (6) and (8) through (12) are subdivided into two columns for orbits 43 and 117, one each for channels 2 and 4. All

other orbits refer to channel 2 only. Columns (2) and (3) give respectively the orbit number and approximate geographical location of the viewed area. Column (4) gives the shelter temperature, either directly recorded by ground or ship station, or, in the cases of orbits 581 and 624, inferred from bucket temperatures recorded by various ships. Column (5) gives the estimated surface temperatures as described above. Column (6) gives the equivalent blackbody temperatures as determined from TIROS III channel 2 and channel 4 observations, averaged over the relevant geographical areas. Column (7) gives the total precipitable water vapor content. Column (8) gives the equivalent blackbody temperatures computed theoretically for the relevant model atmospheres. Column (9) gives the difference [T_{BB} (computed) $-T'_{BB}$ (measured)] of columns (8) and (6). Column (10) gives the corrections, δT_{BB}, which must be applied to the measured blackbody temperatures due to degradation; δT_{BB} values were obtained from Figs. 2 and 3 for the relevant orbit number and measured blackbody temperature. Column (11) gives the corrected measured temperature. The final difference between the computed equivalent blackbody temperature and the measured temperature, corrected for degradation, is given in column (12).

We see from column (12) that the derived corrections for degradation bring the observed temperatures into quite remarkable agreement with theory, in view of the fact that the corrections applied amount to as much as 25°K. Even though the agreement may be fortuitous (e.g., the theory could give temperatures systematically off by 5°K or so due to aerosol absorption and emission, incorrect surface emissivities, etc.), we may conclude from the results that degradation on the whole appears to be properly accounted for, at least for the TIROS III channel 2 radiometer. The results for channel 4 are less certain due to the low number of cases, but in the two shown, the corrections appear to be valid.

IX. NORMALIZING MODELS FOR THE REFLECTED SOLAR RADIATION CHANNELS

The discussion in Section 4.5 concludes that it is impossible to extrapolate the channel 3 and channel 5 data of Fig. 8 back to the ordinate with any degree of confidence, in contrast to the thermal data from channels 2 and 4. The quasi-global albedos inferred from channels 2 and 4 in Section 4.5 were comparable to, although somewhat lower than, the 33.5% annual quasi-global albedo calculated from London (Reference 3). However, because of the uncertainties involved in the albedos inferred from channels 2 and 4, it was decided to attempt to "correct" for much of the instrumental degradation by "normalizing" the channel 3 and channel 5 data to Reference 3.

The normalized average zonal absorbed insolation measured by TIROS, I_{TIROS} can be expressed by

$$I_{TIROS} = \frac{S[1 - \kappa A_{zonal\ ave}'] \times Q}{2\pi R_e^2 \, (sin\zeta_2 - sin\zeta_1)} \tag{9.1}$$

where

I_{TIROS} = average zonal absorbed insolation corrected by factor κ (g cal cm^{-2} min^{-1})

S = solar constant (2.0 g cal cm^{-2} min^{-1})

κ = instrumental degradation normalizing factor

$A_{zonal\ ave}'$ = measured average zonal albedo

c) Determine $\overline{W}_{space}'^{(i)}$ corresponding to T_{BB} from Fig. 7 of the Manual.

d) Determine $\overline{W}^{S(i)}$ corresponding to T_C from Fig. 7 of the Manual.

e) Calculate C^F from the formula [cf. Eq. (8.2)].

$$C^{F(i)} = \frac{\overline{W}^{S(i)} - \overline{W}_{space}'^{(i)}}{\overline{W}^{S(i)}} \qquad (8.3)$$

The housing temperature, T_C, used above may be obtained for any orbit i from Fig. 16 of the Manual.

The correction nomograms in Figs. 1a and 1b were constructed in the following manner:

From Eq. (8.1) the equations relating the measured effective radiant emittance on orbit i to the calibrated effective radiant emittance are given by

$$\overline{W}'^{(i)} = C^{F(i)}\overline{W}^F + (1 - C^{F(i)})\ \overline{W}^{S(i)}$$

and $\qquad\qquad\qquad\qquad\qquad\qquad\qquad\qquad\qquad\qquad\qquad\qquad (8.4)$

$$\overline{W}'^{(i)} = \overline{W}^W - (1 - C^{F(i)})\ \overline{W}^{S(i)}$$

for the floor and wall sides, respectively, where $C^{W(i)} = 1$. In Eq. (8.4) it was assumed that the right-hand side of Eq. (8.1) remains positive upon removal of the absolute value sign, a condition which, in fact, was later verified for all cases of interest through orbit 118.

The following steps were then carried out:

(1) Measured equivalent blackbody temperatures were assumed ranging from $T_{BB}' = 190°K$ to $T_{BB}' = 280°K$ in increments of $10°K$. These temperatures cover the range of interest for channel 1.

(2) Values of the measured effective radiant emittances, $\overline{W}'$, were obtained from the corresponding values of T_{BB}' from Fig. 7 of the Manual.

(3) Corresponding values of the calibrated effective radiant emittances, $\overline{W}^F$ and $\overline{W}^W$, were calculated with the aid of Eq. (8.4). These calculations were repeated for every ten orbits using the pertinent values of $C^{F(i)}$ and $\overline{W}^{S(i)}$, previously determined.

(4) Finally, equivalent blackbody temperatures, T_{BB}, corresponding to $\overline{W}^F$ and $\overline{W}^W$ were obtained from Fig. 7 of the Manual.

(5) The equivalent blackbody temperature difference, $\delta T_{BB} = T_{BB} - T_{BB}'$, was then computed for each selected value of T_{BB}' and orbit number, i. The resulting nomograms (Figs. 1a and 1b) were then constructed with the aid of considerable smoothing.

The estimated absolute accuracy given in the Manual is revised to read ±5 to $\pm10°K$ up to orbit 118 after applying corrections from Fig. 1.

8.2 Channel 2

Asymmetrical degradation does not become a problem until about orbit 875 for channel 2. Beyond this orbit Δf exceeds 2 cps (cf. Fig. 54 in the Manual). The channel 2 correction nomogram, which is valid only through orbit 875, was constructed with the approximation that Δf is identically zero. Thus, only symmetrical optical degradation need be considered.

Unlike the case for channel 1, in addition to the observed space-viewed level we have another relation between the symmetrical degradation constant, $C^i = C^{W(i)} = C^{F(i)}$, which can be obtained through a determination of the quasi-global emitted radiant power, P^i, as discussed in Section V. From Eq. (6.4) we obtain the relation for channel 2

$$\overline{W}_{ave}{}^i = \frac{P^i}{15.168 \times 10^{14}} - 25.482 \tag{8.5}$$

The critical nature of extrapolating the data in Fig. (10) back to the ordinate to determine P^o is emphasized once again. It is seen in Eq. (8.7) that P^o establishes the "undegraded standard" on which all corrections are subsequently based, and to the extent that it is in error, all derived corrections will also be in error.

From Eq. (8.1), together with Eq. (8.5) and approximation (3) in Section V, we have

$$\frac{\overline{W}'^{(i)}}{\overline{W}} = C^i = \frac{\overline{W}_{ave}{}^i}{\overline{W}_{ave}{}^o} \tag{8.6}$$

Combining Eq. (8.5) and Eq. (8.6) we obtain

$$\overline{W}'^{(i)} = \overline{W}\, \frac{\overline{W}_{ave}{}^i}{\overline{W}_{ave}{}^o} = \overline{W}\, \frac{\dfrac{P^i}{15.168 \times 10^{14}} - 25.482}{\dfrac{P^o}{15.168 \times 10^{14}} - 25.482}\,, \tag{8.7}$$

or,

$$\overline{W}'^{(i)} = \overline{W}\, \frac{P^i - 386.511 \times 10^{14}}{P^o - 386.511 \times 10^{14}}$$

The procedure for constructing the channel 2 correction nomogram was as follows:

(1) Measured equivalent blackbody temperatures were assumed ranging from $T_{BB}' = 180°K$ to $T_{BB}' = 320°K$ in increments of $20°K$.

(2) Values of the measured effective radiant emittances, $\overline{W}'$, were obtained from the corresponding values of T_{BB}' from Fig. 8 of the Manual.

(3) Values of P^i were read off Fig. 10 corresponding to every 50 orbits in the range $0 \leq i \leq 900$ orbits.

(4) Corresponding undegraded values of $\overline{W}$ were calculated from the relevant values of $\overline{W}'^{(i)}$ and P^i with the aid of Eq. (8.7).

(5) Equivalent blackbody temperatures, T_{BB}, were determined for each value of $\overline{W}$ from Fig. 8 of the Manual.

(6) The differences, $\delta T_{BB} = T_{BB} - T_{BB}'$, are determined for each value of T_{BB}' as a function of orbit number, i. The resulting nomogram is a one-parameter family of curves as given in Fig. 2. The estimated absolute accuracy given in the Manual is revised to read $\pm 4°$ to $\pm 8°K$ up to orbit 875 after applying corrections from Fig. 2.

8.3 *Channel 4*

The difference between the observed and calibrated space-viewed levels (Δf) is negligible through orbit 130 (cf. Fig. 55 of the Manual). For this reason the symmetrical

TABLE II

TIROS III CASE STUDIES OF CHANNELS 2 AND 4

CLEAR SKIES

(1) Date	(2) Orbit	(3) Location	(4) Shelter Temp. (°K)	(5) Estimated Surface Temp. (°K)	(6) T_{BB}' (°K) (measured)		(7) Total Precip. H_2O (cm)	(8) T_{BB} (°K) (computed)*		(9) ΔT_{BB} (°K) [(8)−(6)]		(10) δT_{BB} (°K)		(11) Corrected T_{BB}' (°K) [(6)+(10)]		(12) Corrected ΔT_{BB} (°K) [(8)−(11)]	
					C2	C4		C2	C4	C2	C4	C2	C4	C2	C4	C2	C4
7-15-61	43	Sahara Desert	310.0	335-320	310	287	1.181	322-310	298-288	+12, 0	+11, +1	+4.5	+3	314.5	290	+7.5, −4.5	+8, −2
7-20-61	117	Atlantic Ocean, off Surinam, S.A.	299.0	300.8	276	264	5.018	287	271	+11	+7	+7.7	+6	283.7	270	+3.3	+1
8-21-61	581	Pacific Ocean, off Baja Calif.	294.3	294.3	266		5.756	287		+21		+23		289		−2.0	
8-22-61	595	Amarillo, Texas	299.5	304.5	274		2.202	294		+20		+24		298		−4.0	
8-23-61	609	Dodge City, Kansas	298.2	303.2	272		1.811	294		+22		+24		294		−2.0	
8-24-61	623	Oklahoma City, Oklahoma	302.0	307.0	270		2.764	295		+25		+24		294		+1.0	
8-24-61	624	Pacific Ocean, off San Francisco, Calif.	293.0	292.8	258		2.029	286		+28		+23		281		+5.0	
8-26-61	651	Oklahoma City, Oklahoma	304.5	309.5	268		2.585	294		+26		+25		293		+1.0	

*Assuming emissivity of surface = 1.0

Q = zonal illuminated area cross-section (meter^2)

R_e = radius of the Earth (6,371,200 meters)

ζ_2 = northern zonal boundary latitude

$\zeta_1 = \zeta_2 - 10°$

From Eq. (9.1) the TIROS III albedo values were converted to average zonal absorbed insolation values. These values were then plotted versus latitude where the scale was drawn in proportion to the sine of the latitude, thus weighting the latitude coordinate according to the actual zonal areas on Earth. Absorbed insolation values determined from Reference 3 for the northern hemisphere at a comparable time of year were plotted on the same graph. Values for the opposite season from that in the northern hemisphere were used for the southern hemisphere. For example, the absorbed insolation values for July in the zone S10° to S20° were taken from Reference 3 winter data for the zone N10° to N20°. Six curves of absorption versus latitude were plotted for each channel in this manner, one for each 9-day period, eliminating the last two periods because of very noisy data. These curves are shown in Figures 18a through 19f.

By planimetering the area under the curve of TIROS data and that of Reference 3 data over comparable zonal regions, one can determine the factor, κ, necessary to cause the area under the TIROS curve to be equivalent to the area under the Reference 3 curve. The equivalence determined by the factor κ can be expressed by

$$2\pi R_e^2 \int_{\zeta_S}^{\zeta_N} I_{LONDON}(\zeta)\cos\zeta d\zeta = 2\pi R_e^2 \int_{\zeta_S}^{\zeta_N} I_{TIROS}(\zeta)\cos\zeta d\zeta \qquad (9.2)$$

where

$I_{LONDON}(\zeta)$ = average absorbed insolation according to Reference 3 (g cal cm^{-2} min^{-1})

$I_{TIROS}(\zeta)$ = average absorbed insolation from normalized TIROS measurements, graphically determined using Eq. (9.1)

ζ_N = northern bounding latitude of region where TIROS data were acquired

ζ_S = southern bounding latitude of region where TIROS data were acquired

The degradation normalizing factors, κ^i, thus determined in Figs. 18a through 19f, were plotted versus orbit number in Figs. 4 and 5 for channels 3 and 5, respectively. Each value of κ^i was assumed to prevail at the midpoint orbit in the nine-day period over which each value of A^c was calculated. The greater scatter of the first three points in Fig. 4 compared to those in Fig. 5 is puzzling. A recheck of the data disclosed no data-processing errors, and we can offer no other satisfactory explanation of the discrepancy.

The results of our limited analysis of channels 3 and 5, although containing appreciable scatter, indicate that especially severe degradation in the response of channel 5 occurred. It has been subjectively determined that for values of κ^i larger than $\sim$5, even relative mapped patterns from the short wave channels become of limited value due to excessive noise in the data. Thus, after orbit 300, the channel 5 data are of limited value (cf. Fig. 5), and only channel 3 data are recommended for such purposes as the mapping of cloud patterns occurring in later orbits up to about orbit 875 when excessive noise also limits their value (cf. Fig. 4). Because of the limited scope of our investigations to date and because of the technique employed of normalizing the short wave channel data to Reference 3, no estimate of the absolute accuracy of the normalized channel 3 and channel 5 data is possible.
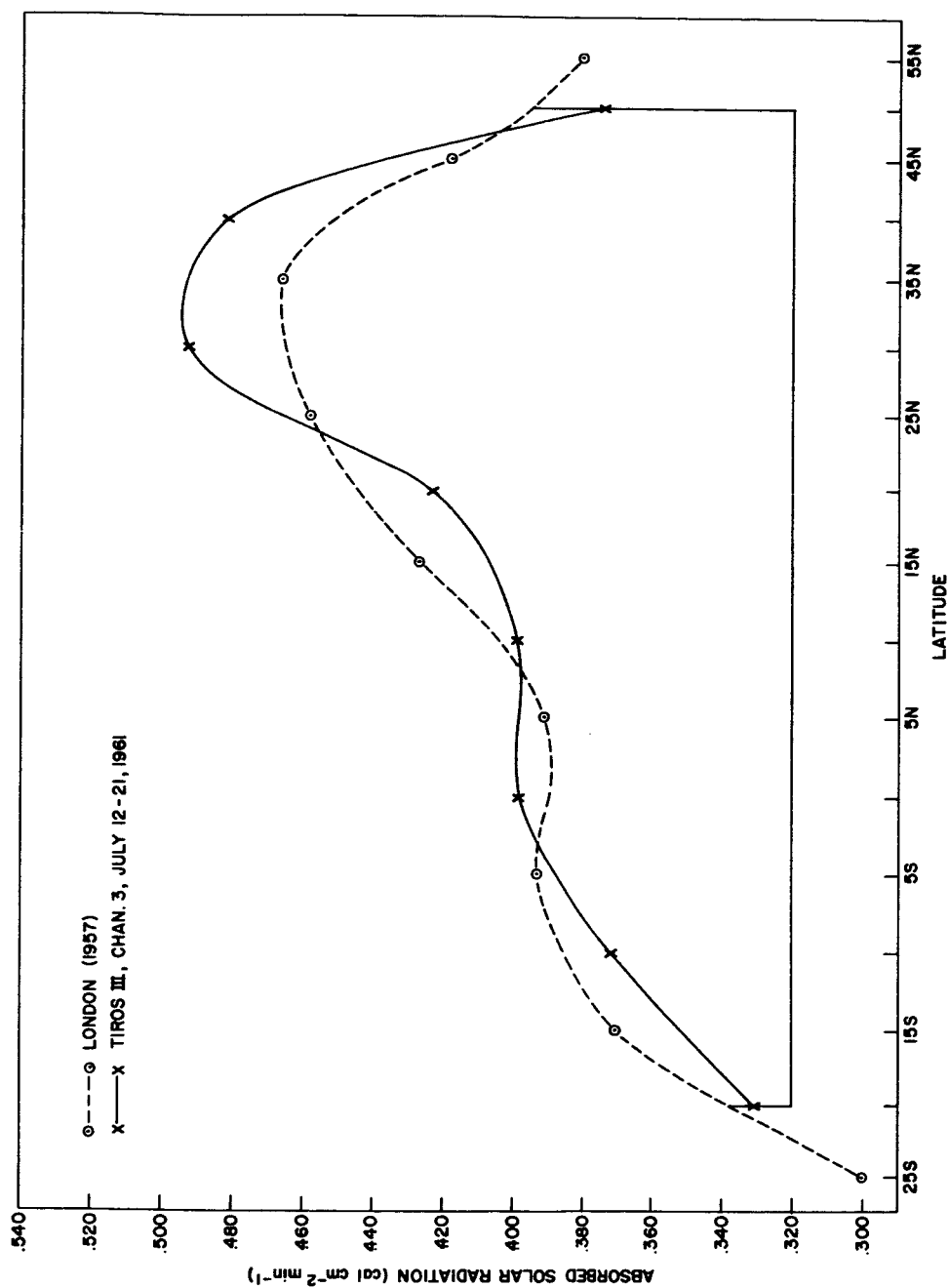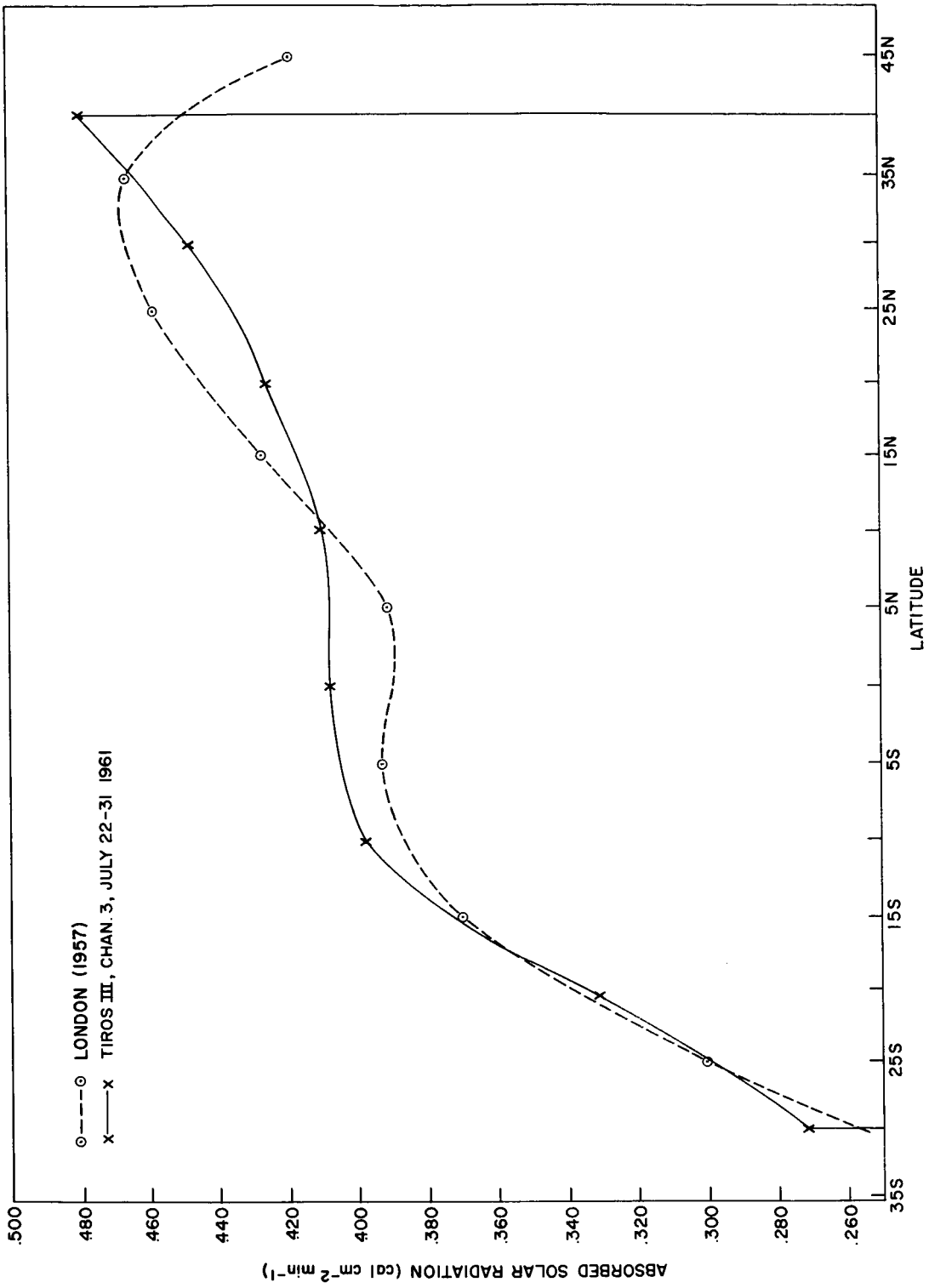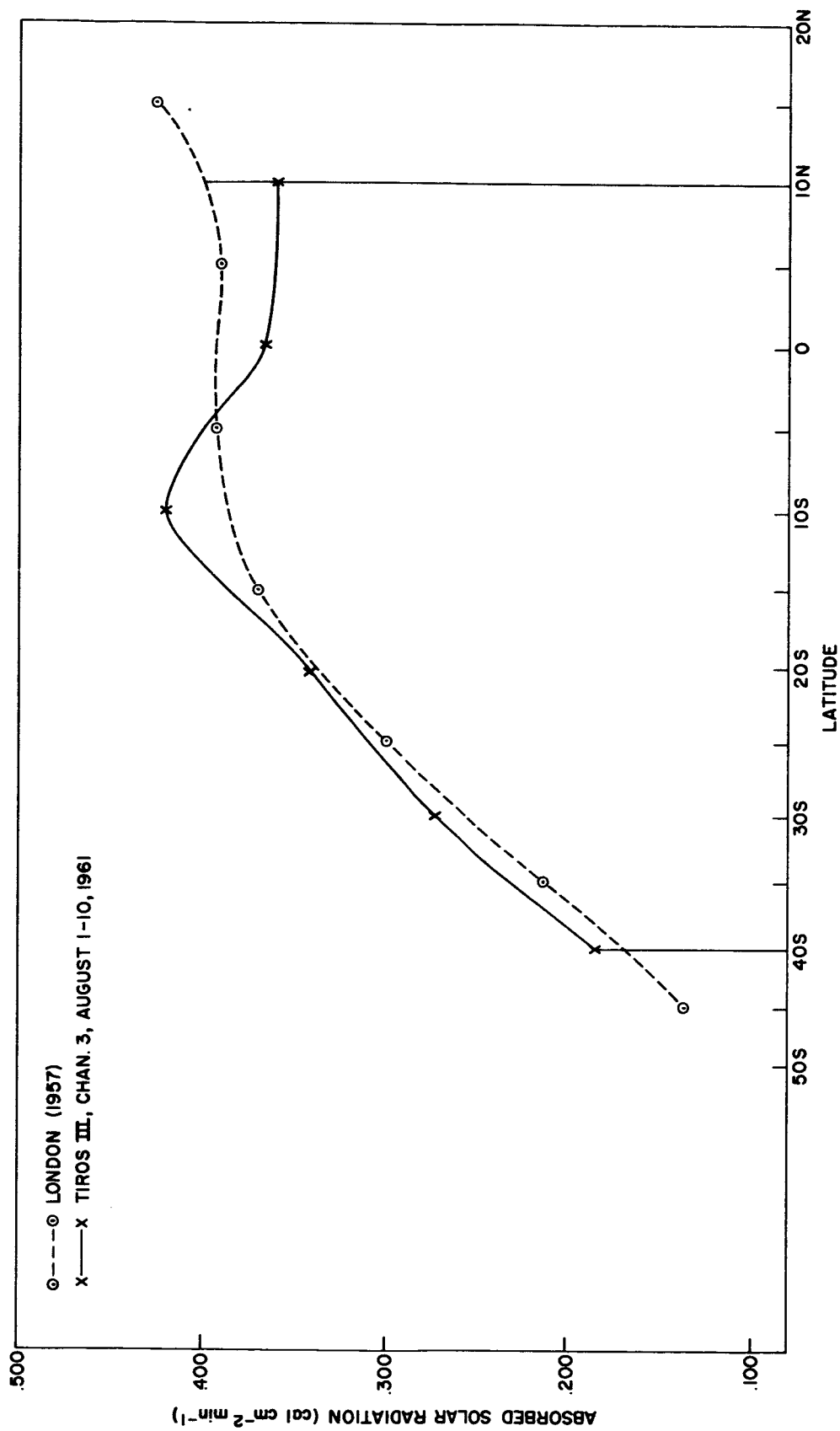
42

Figure 18—Absorbed insolation plotted as a function of latitude, normalizing the TIROS III, channel 3 data to Reference 3 (London). The abscissa was drawn in proportion to the sine of the latitude, thus weighting the zones according to their areas on Earth. For the period 12 July–21 August 1961, London's summer data were used for the northern hemisphere and winter data for the southern hemisphere. For the period 22 August–8 September 1961, an average of London's summer and fall data was used for the northern hemisphere and an average of winter and spring data for the southern hemisphere.

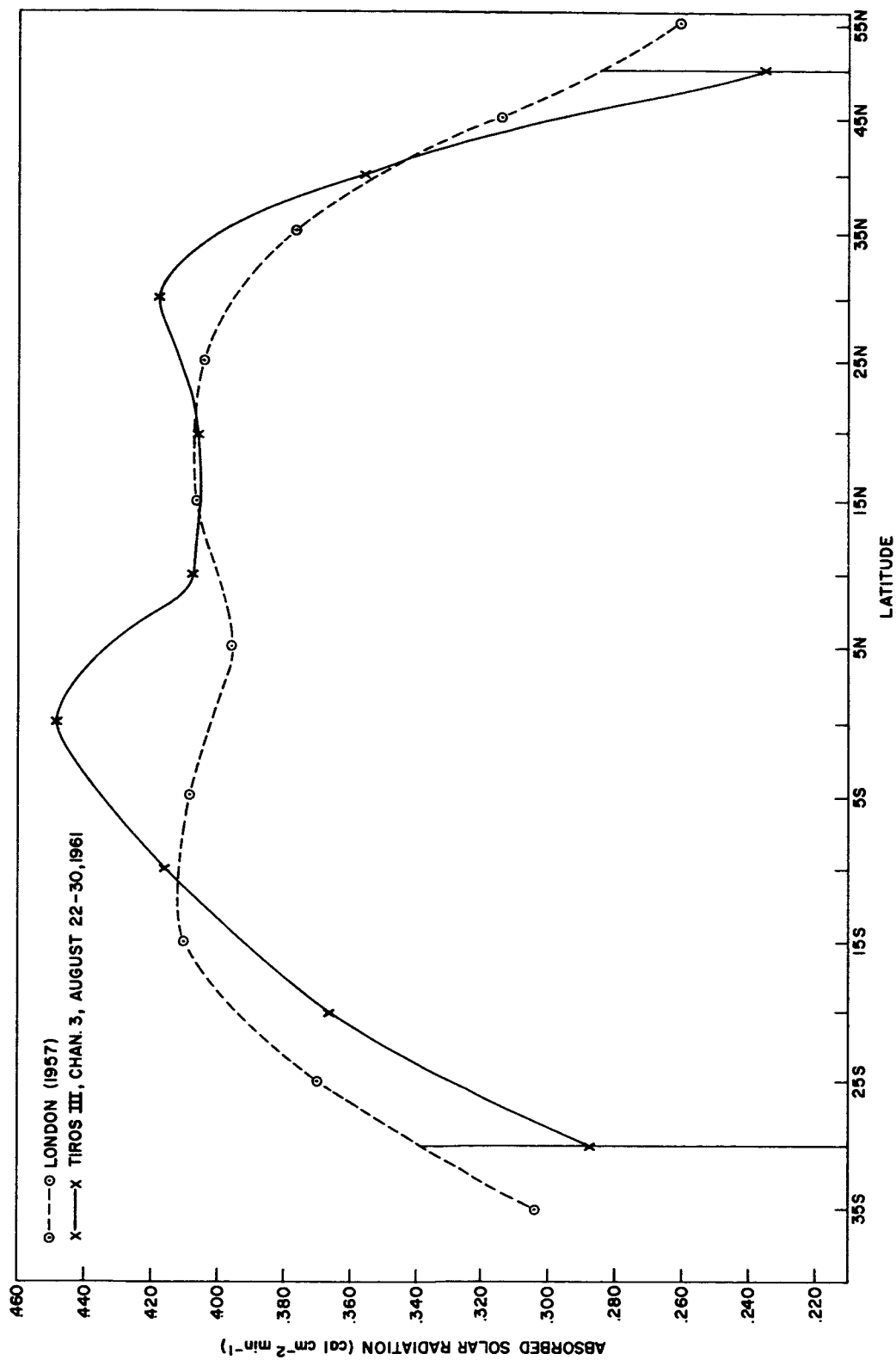(a) TIROS data during the period 12–21 July 1961 have been normalized by the factor, $\kappa = 2.4$.

43

(b) TIROS data during the period 22–31 July 1961 have been normalized by the factor, $\kappa = 3.0$.
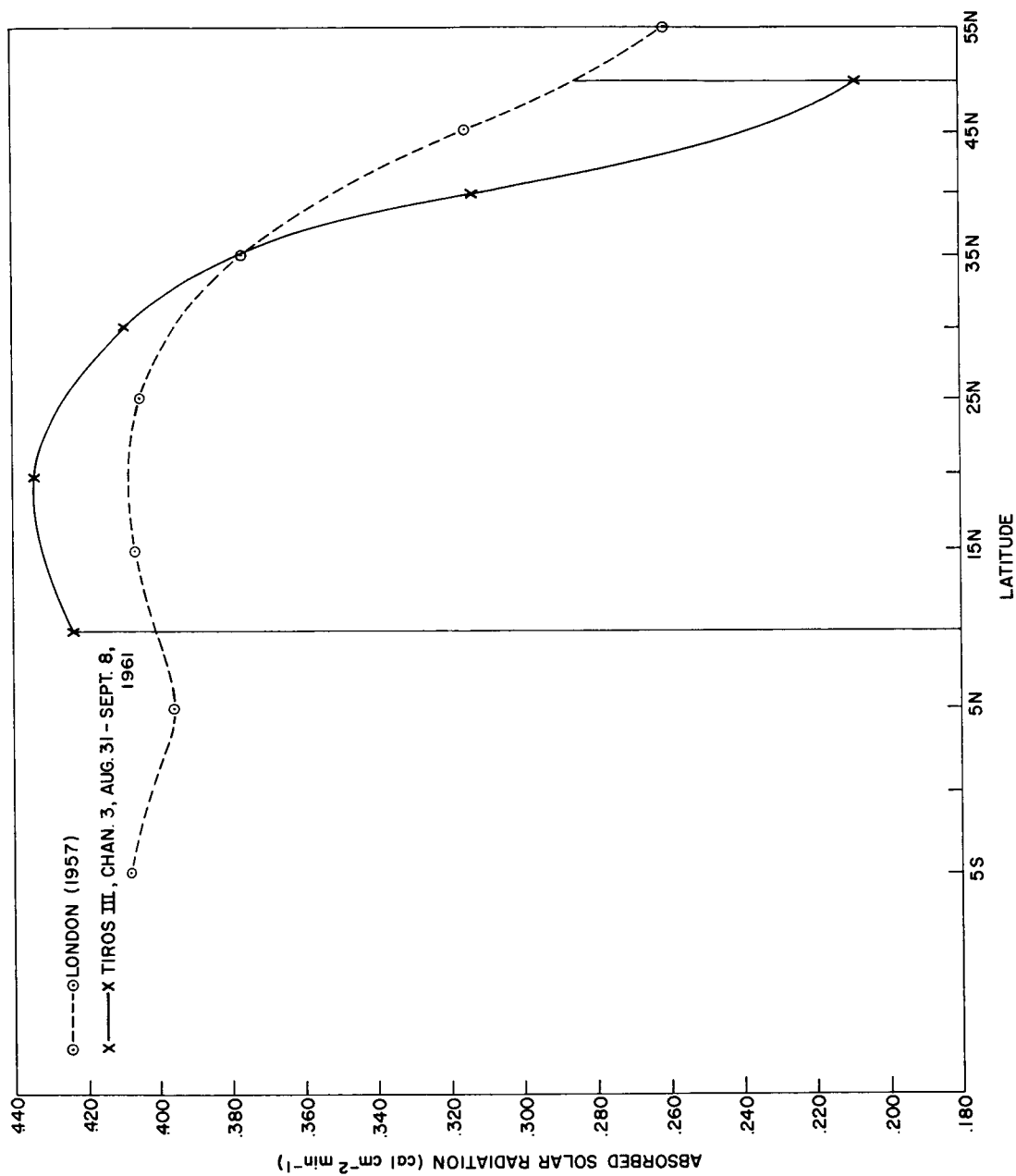
44

(c) TIROS data during the period 1-10 August 1961 have been normalized by the factor, $\kappa = 2.6$.

⊙─ ─ ─⊙ LONDON (1957)

×───× TIROS III, CHAN. 3, AUGUST 1-10, 1961

ABSORBED SOLAR RADIATION (cal cm^{-2} min^{-1})

LATITUDE

45

(d) TIROS data during the period 10–21 August 1961 have been normalized by the factor, $\kappa = 4.3$.

46

(e) TIROS data during the period 22–30 August 1961 have been normalized by the factor, $\kappa = 4.1$.

47

(f) TIROS data during the period 31 August–8 September 1961 have been normalized by the factor, $\kappa = 4.5$.
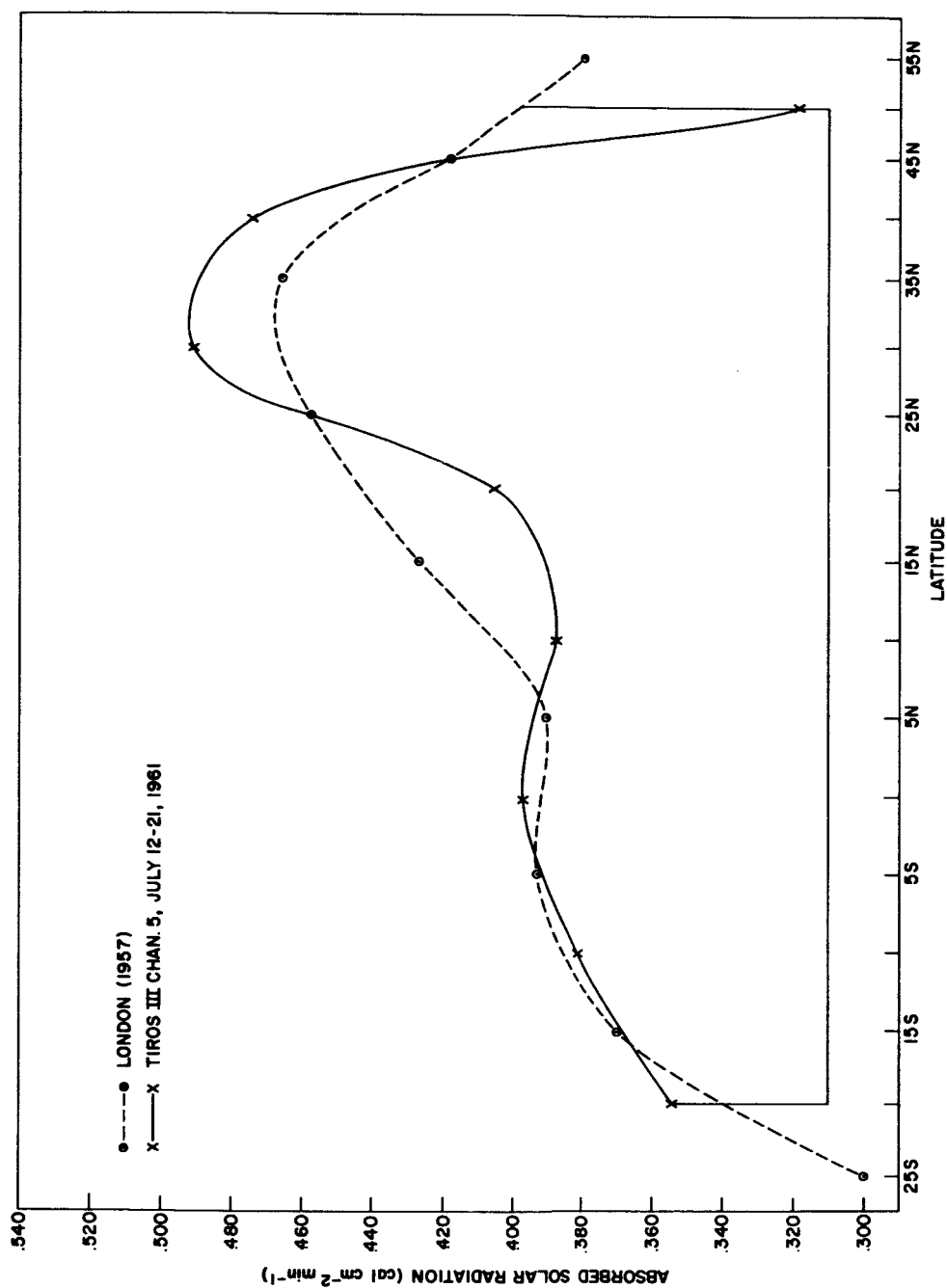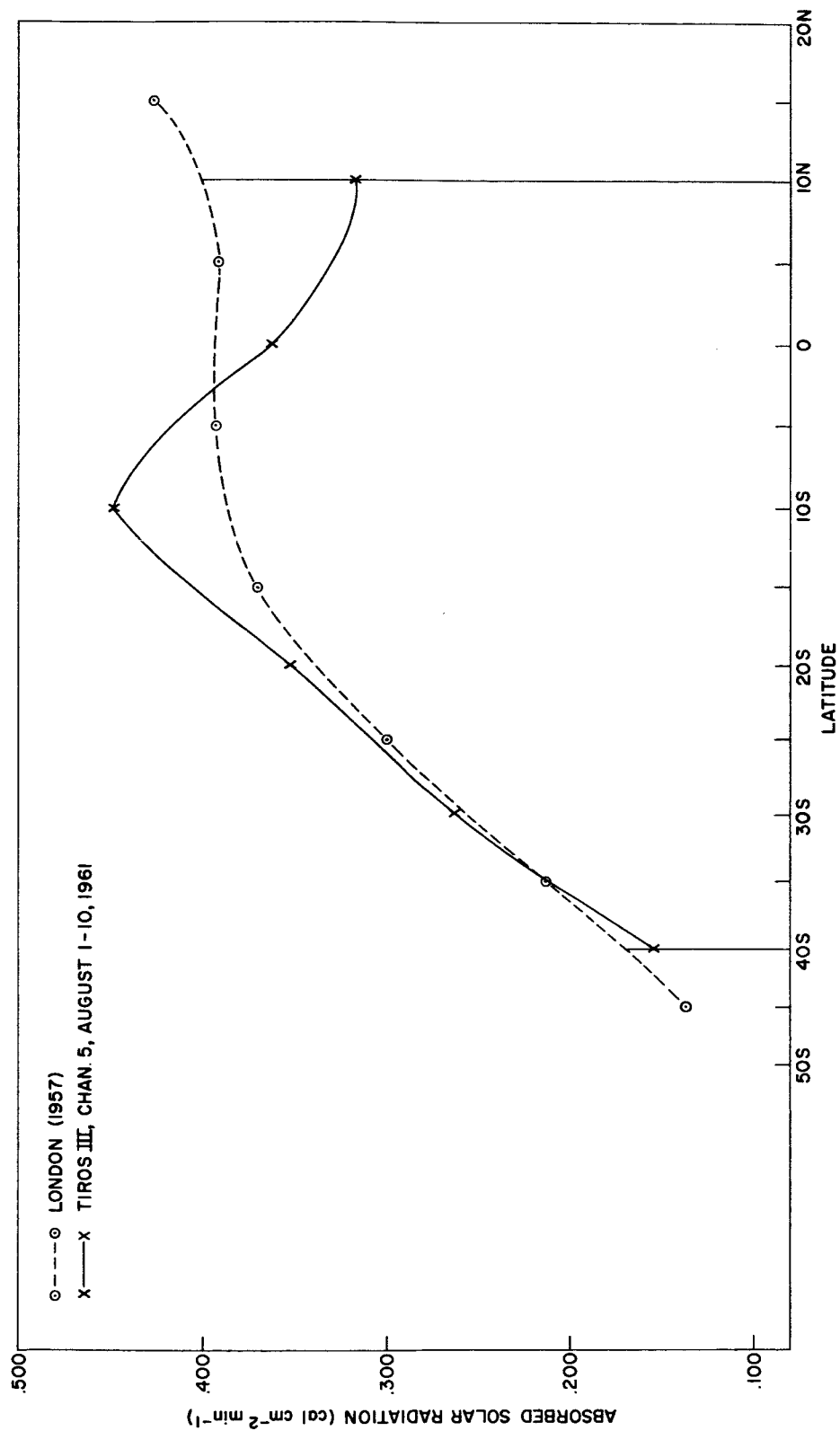
48

Figure 19—Absorbed insolation plotted as a function of latitude, normalizing the TIROS III, channel 5 data to Reference 3 (London). The abscissa was drawn in proportion to the sine of the latitude, thus weighting the zones according to their areas on Earth. For the period 12 July–21 August 1961, London's summer data were used for the northern hemisphere and winter data for the southern hemisphere. For the period 22 August–8 September 1961, an average of London's summer and fall data was used for the northern hemisphere and an average of winter and spring data for the southern hemisphere.

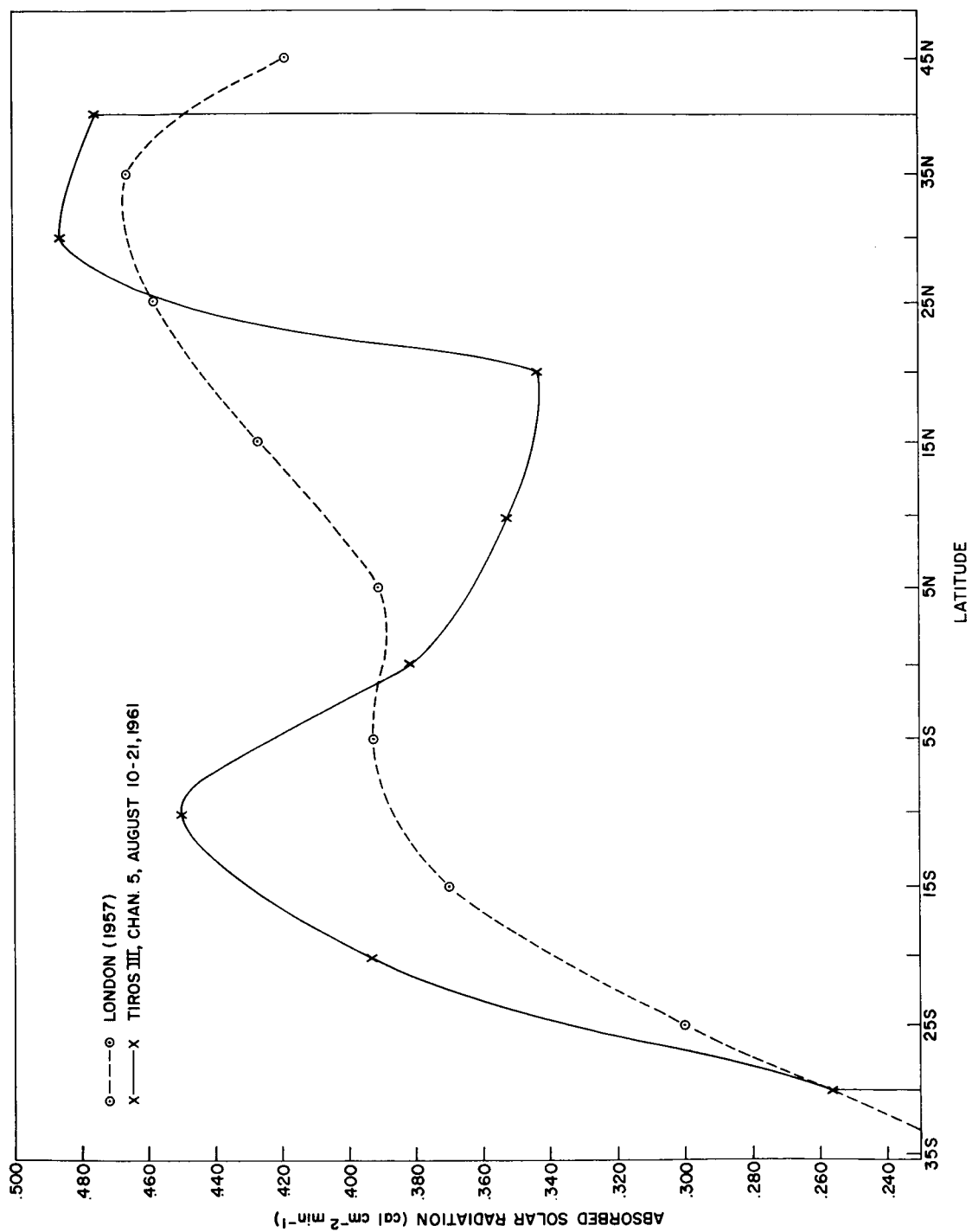(a) TIROS data during the period 12–21 July 1961 have been normalized by the factor, $\kappa = 2.6$.

49
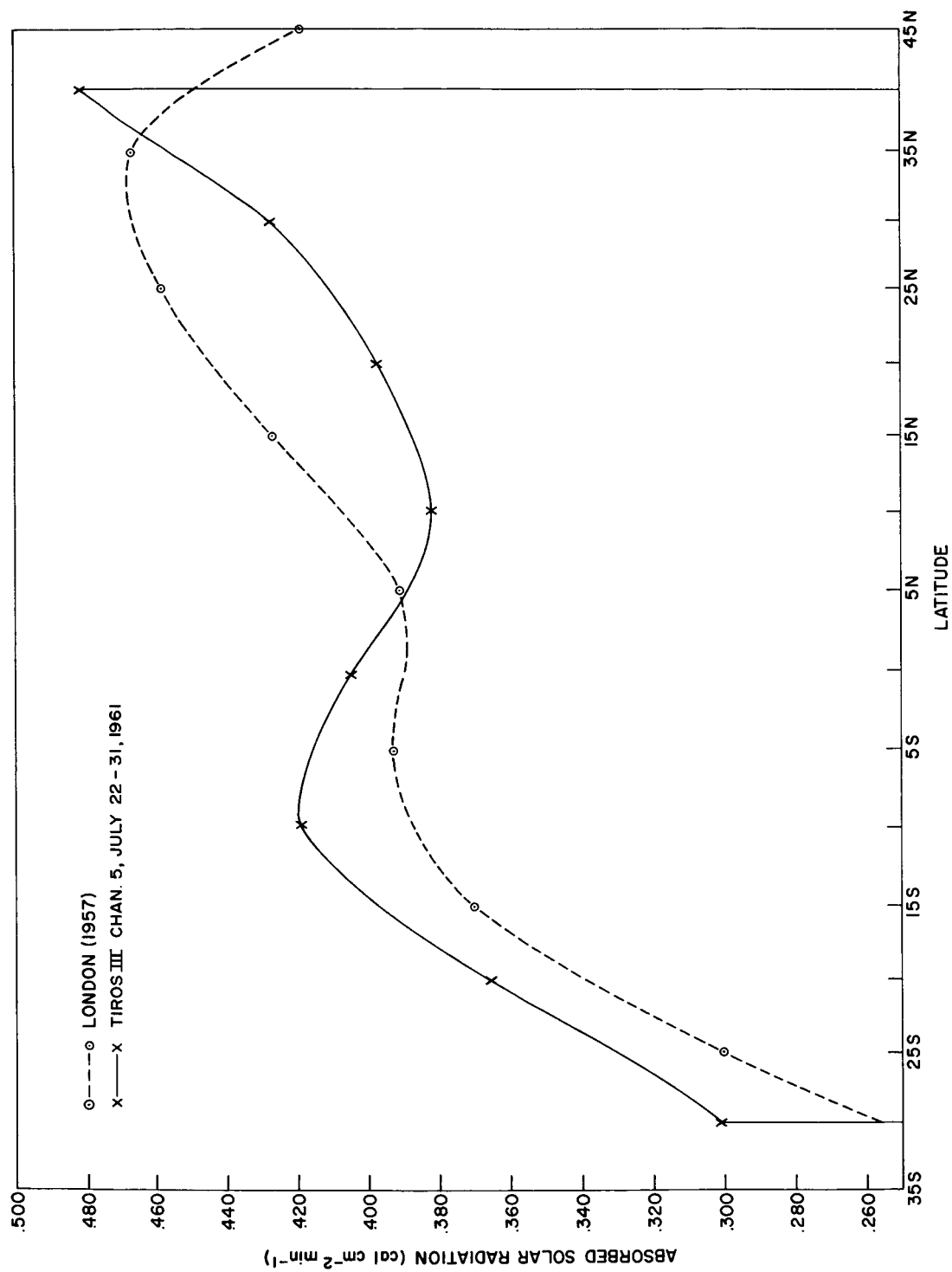
(b) TIROS data during the period 22–31 July 1961 have been normalized by the factor, $\kappa = 3.9$.
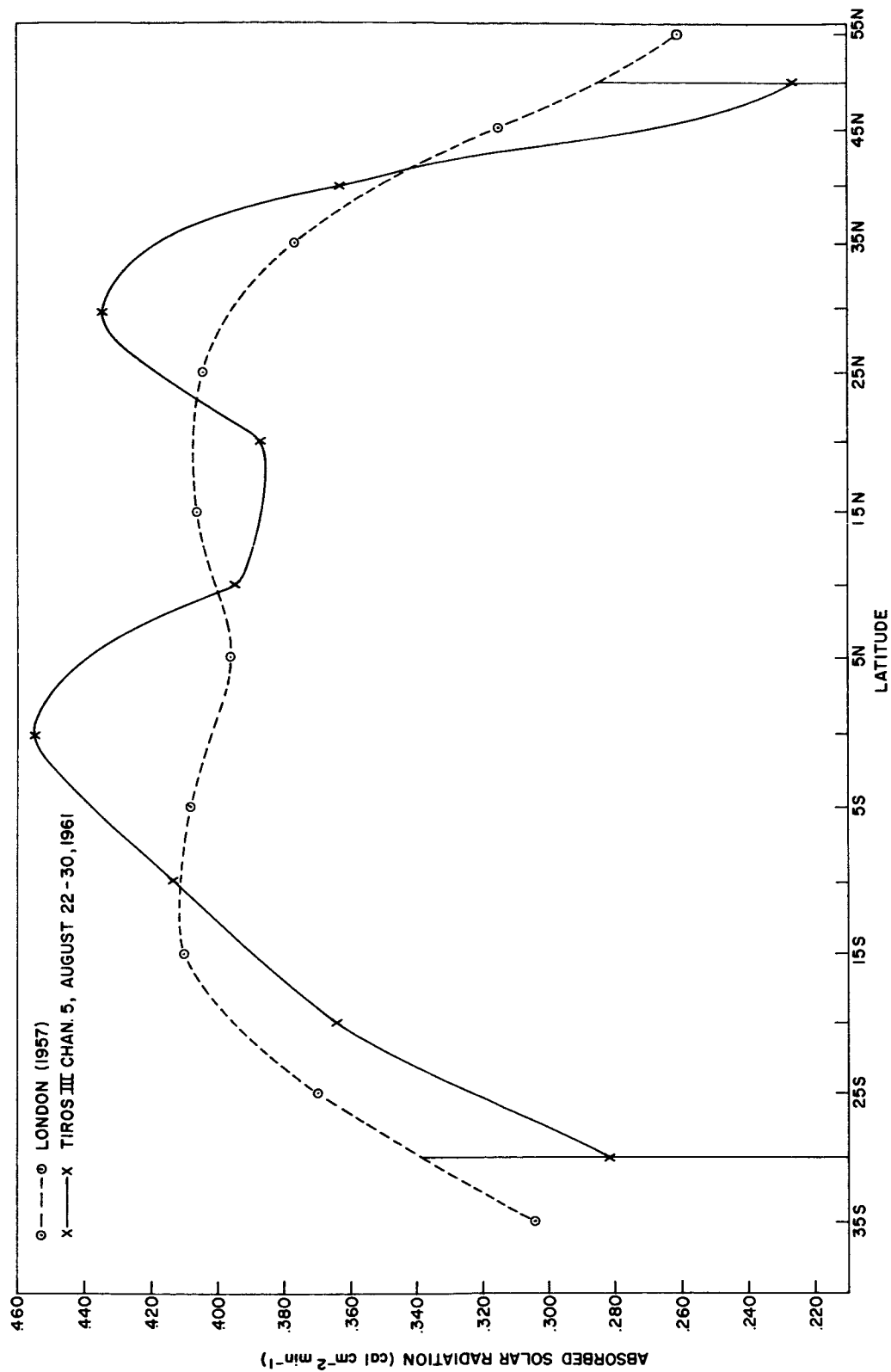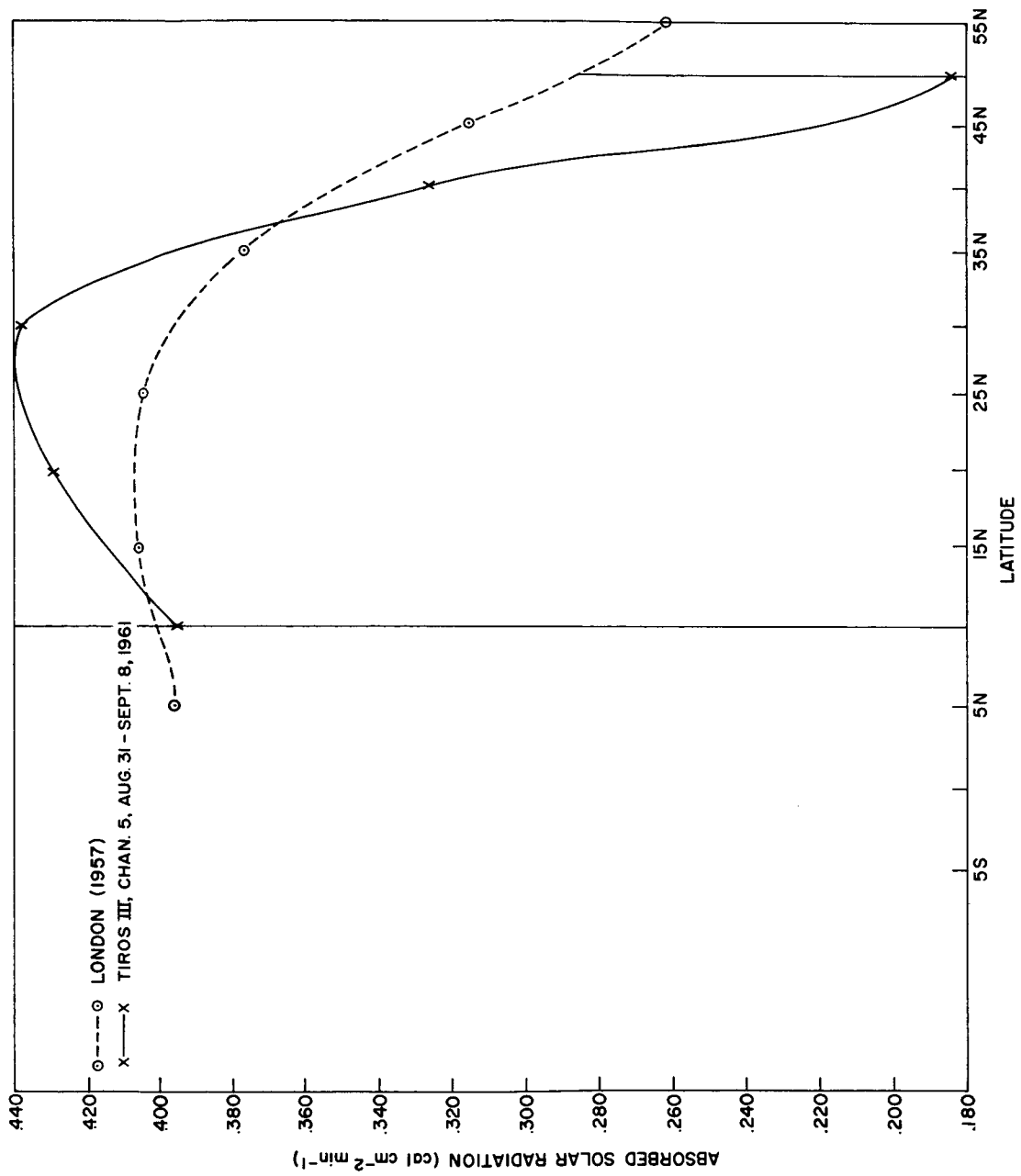
50

(c) TIROS data during the period 1–10 August 1961 have been normalized by the factor, $\kappa = 5.5$.

51

(d) TIROS data during the period 10–21 August 1961 have been normalized by the factor, $\kappa = 9.4$.

52

(e) TIROS data during the period 22–30 August 1961 have been normalized by the factor, $\kappa = 8.2$.

53

(f) TIROS data during the period 31 August–8 September 1961 havc been normalized by the factor, $\kappa = 9.1$.

54

X. CONCLUSIONS

The responses of all channels of the TIROS III five-channel radiometer were observed to degrade rapidly after launch. There was no on-board calibration for the radiometers except for the observed space-viewed level, but by making certain broad assumptions it was possible to derive correction models for the thermal channels which we believe account for much of the apparent degradation occurring in the instrumental response.

The determination of correction models for the short-wave channels presented a much more difficult task for several reasons. Three of these are:

1. The problem of radiative transfer in the visible region of the spectrum in the atmosphere is much more complex than in the infrared. There is a lack of knowledge of the overall magnitude and anisotropic character of the reflectance from various cloud and ground surfaces. Furthermore, no applicable theory of large particle scattering in the atmosphere is yet available, and we do not know what the turbidity profiles are. Hence, the technique of "working backwards", i.e., comparing individual satellite observations with theoretical calculations of what the sensors should see, as was done for channels 2 and 4, is virtually impossible.

2. The problem of adequate sampling in space and time and over all combinations of solar incidence and scattering angles is less nearly fulfilled for the short-wave channels than is the comparable problem for the long-wave channels; therefore, the assumption of constancy in the quasi-global albedo is probably less valid than it is for quasi-global emitted radiation.

3. The original calibration in the laboratory, involving integrations over lamps having a different color temperature from that of the sun, and involving reflecting surfaces whose spectral reflectivities and angular intensity variations must be accounted for in the calculations, contains greater uncertainties than the relatively simple calibration of the thermal channels, using blackbody targets.

The corrections for channels 2 and 4 and the normalizing factors for channels 3 and 5 were based upon analyses of averages of many measurements covering nearly the entire dynamic range of the instrument. Such mean values must be used cautiously in attempting to correct individual measurements. For example, the danger of applying the normalizing factors for channels 3 and 5 to individual measurements deviating considerably from the mean is clearly evident in Fig. 9.

Further statistical investigations of the degradation problem will be made looking into the frequency distributions of individual measurements about the mean. Also, statistical analyses of the backscattering of solar radiation as a funciton of solar zenith angle, sensor zenith angle, relative azimuth, and "scattering angle" will be made with the data to investigate the possible shortcomings of the simple cosine reflectance law assumed above. But it is felt that it is appropriate to publish now the results of our work to date for the immediate information and use of recipients of the "TIROS III Radiation Data Catalog".[2]

The correction procedures discussed in this Supplement are at best only approximations, and a satisfactory solution to the instrumental degradation problem can only be achieved with a means of periodically calibrating the sensors while in orbit. Plans are now proceeding to include on-board calibration on the next medium-resolution radiation experiment to be flown after TIROS VII, which is presently in orbit.

Finally, it is emphasized that the data from all channels are of value for such purposes as the relative mapping of cloud systems up to the orbit numbers listed in Sections VIII and IX for the respective channels, viz., orbits 118 for channel 1, 875 for channels 2 and 3, 130 for channel 4, and 300 for channel 5.

REFERENCES

1. Staff, Aeronomy and Meteorology Division, Goddard Space Flight Center: "TIROS III Radiation Data Users' Manual". NASA, Goddard Space Flight Center, Greenbelt, Maryland, August, 1962, 71 pp.

2. Staff, Aeronomy and Meteorology Division, Goddard Space Flight Center and Staff, Meteorological Satellite Laboratory, U. S. Weather Bureau: "TIROS III Radiation Data Catalog". NASA, Goddard Space Flight Center, Greenbelt, Maryland, December 15, 1962, 388 pp.

3. London, Julius: "A Study of the Atmospheric Heat Balance". *Final Report, Contract AF 19 (122)–165*, Department of Meteorology and Oceanography, New York University, July, 1957.

4. Wark, D. Q., G. Yamamoto, and J. H. Lienesch: "Infrared Flux and Surface Temperature Determinations from TIROS Radiometer Measurements". Meteorological Satellite Laboratory *Report No. 10*, U. S. Weather Bureau, National Weather Satellite Center, Washington, D.C., August, 1962. (Also "Methods of Estimating Infrared Flux and Surface Temperature from Meteorological Satellites". *J. Atmos. Sci., 19*, 369–384, September, 1962.)

5. Wark, D. Q., G. Yamamoto, and J. H. Lienesch: "Infrared Flux and Surface Temperature Determinations from TIROS Radiometer Measurements". Meteorological Satellite Laboratory *Supplement to Report No. 10*, U. S. Weather Bureau, National Weather Satellite Center, Washington, D.C., April, 1963.

6. Bandeen, W. R., and W. Nordberg: "Radiation Measurements from TIROS III and TIROS IV and Inferences Regarding the Albedo and Heat Budget of the Earth". *Paper presented at the XIII General Assembly of the IUGG, Berkeley, California, August 28, 1963.*

7. Hanel, R. A. and D. Q. Wark: "TIROS II Radiation Experiment and Its Physical Significance". *J. Opt. Soc. Am., 51*, 1394–1399, December, 1961.

8. Nordberg, W., and W. Smith: "Rocket Measurement of the Structure of the Upper Stratosphere and Mesosphere", pp. 391–408 in *Proceedings of the International Symposium on Stratospheric and Mesospheric Circulation*, Institut für Meteorologie und Geophysik der Freien Universität Berlin, 20–31 August, 1962.

9. Dütsch, H. U.: "Vertical Ozone Distribution over Arosa". *Final Report Contract AF 61 (541)–905 (Ozone and General Circulation in the Stratosphere)*, September, 1959.

10. Manabe, Syukuro, and Fritz Möller: "On the Radiative Equilibrium and Heat Balance of the Atmosphere". *Monthly Weather Review, 89*, 503–532, December, 1961.